

INVESTIGATION OF ELASTIC AND PHOTOELASTIC  
CONSTANTS OF FERROELECTRIC AND  
GLASS MATERIALS USING  
BRILLOUIN SCATTERING

BY

ZHENGDA PAN  
"

Bachelor of Science

Tsuhua(Qinghua) University

Beijing, China

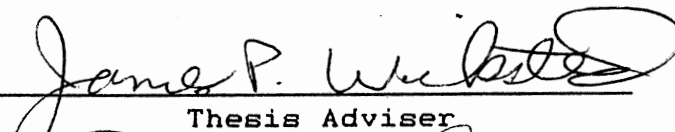
1968

Submitted to the Faculty of the  
Graduate College of the  
Oklahoma State University  
in partial fulfillment of  
the requirements for  
the Degree of  
MASTER OF SCIENCE  
December, 1989

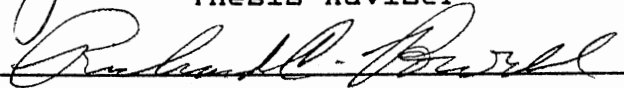
Thesis  
1989  
P187i  
cop. 2

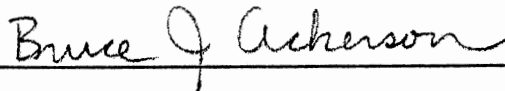
INVESTIGATION OF ELASTIC AND PHOTOELASTIC  
CONSTANTS OF FERROELECTRIC AND  
GLASS MATERIALS USING  
BRILLOUIN SCATTERING

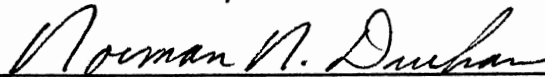
Thesis Approved:

  
\_\_\_\_\_

Thesis Adviser

  
\_\_\_\_\_

  
\_\_\_\_\_

  
\_\_\_\_\_

Dean of the Graduate College

1350211

## ACKNOWLEDGMENTS

First, I would like to express my deep gratitude to my thesis advisor, Dr. J. P. Wicksted for his advice, guidance, and support throughout this project. I would also like to thank Dr. B. J. Ackerson and Dr. R. C. Powell for serving in my thesis committee. Extended thanks go to Dr. G. H. Gangwere for his help during this work and go to Mr. A. Bouchalkha for his growing RADP samples.

I would also like to thank the Physics Department at OSU and especially to thank Dr. L. E. Halliburton and Dr. P. A. Westhaus for their help during my stay in OSU.

Finally, I must thank my parents, my uncle, my wife, and my son for their love and support throughout my life and especially during my studying at Oklahoma State University.

Financial support for this work was provided by Center for Night Vision and Electro-Optics (CNVEO) under a contract # DAAB07-88-C-F407.

## TABLE OF CONTENTS

Chapter	Page
I. INTRODUCTION . . . . .	1
A Historical Survey of Brillouin Scattering. . . . .	1
The Work Reported in This Thesis. . . . .	2
A Review of Previous Work . . . . .	2
II. THEORY . . . . .	6
Thermal Agitation and Brillouin Scattering. . . . .	6
Brillouin Shifts and Elastic Constants of Materials . . . . .	9
Brillouin Scattering Cross Section and Photoelastic Constants of Materials. . . . .	11
Rayleigh and Brillouin Scattering in Glass . . . . .	16
Elastic Constants of Glass . . . . .	20
Brillouin Scattering Cross Section of Glass . . . . .	21
Brillouin Scattering in Lithium Niobate .	24
Elastic Constants of Lithium Niobate	26
Brillouin Scattering Cross Section of Lithium Niobate . . . . .	29
Brillouin Scattering in RADP. . . . .	33
III. EXPERIMENTAL APPARATUS AND PROCEDURE . . . . .	37
Experimental Apparatus . . . . .	37
Argon-ion Laser. . . . .	39
Fabry-Perot Interferometer . . . . .	39
Photomultiplier . . . . .	40
Multichannel Analyzer (MCA). . . . .	40
Experiment Procedure . . . . .	40
Sample Preparation . . . . .	40
Setting the Free Spectral Range. . .	48
Choosing the Fore Pinhole and Laser Filter . . . . .	48
Determination of Measured Quantities	49
Weak TA Signal Detection . . . . .	49

IV. RESULTS AND ANALYSIS . . . . .	56
Fluoride Glasses . . . . .	56
Lithium Niobate . . . . .	68
RADP . . . . .	77
V. SUMMARY . . . . .	86
REFERENCES . . . . .	89
APPENDIX A - THE TRANSMISSION FACTOR ( $f_1$ ) AND THE SOLID ANGLE CORRECTION FACTOR ( $f_2$ ). . . . .	93
APPENDIX B - THE FORMULAS FOR DETERMINING THE PHOTOELASTIC CONSTANTS. . . . .	97

## LIST OF TABLES

Table	Page
I. The Densities and the Refractive Indices of the Samples . . . . .	47
II. The Constituents of Two Fluoride Glass Samples (Mol. Percentage). . . . .	66
III. Basic Measured Quantities in Brillouin Scattering (Glasses) . . . . .	66
IV. Sound Velocities, Elastic Constants and Poisson's Ratios ( $\sigma$ ) of Two Fluoride Glasses and Fused Quartz . . . . .	67
V. Photoelastic Constants and Scattering Losses of Two Fluoride Glasses and Fused Quartz . .	67
VI. The Basic Measured Quantities in Brillouin Scattering (Lithium Niobate) . . . . .	73
VII. Sound Velocities and Elastic Constants (Lithium Niobate). . . . .	74
VIII. Photoelastic Constants $P_{31}$ and $P_{41}$ (Lithium Niobate). . . . .	74
IX. The Acousto-Optic Figures of Merit (Lithium Niobate and Fused Quartz) . . . . .	76
X. The Basic Measured Quantities in Brillouin Scattering ( $\text{Rb}_{1-x}(\text{NH}_4)_x\text{H}_2\text{PO}_4$ ). . . . .	84
XI. Sound Velocities and Elastic Constants of RADP. . . . .	85
XII. Photoelastic Constants of RADP . . . . .	85

## LIST OF FIGURES

Figure	Page
1. Light Scattered by Inhomogeneous Patterns in a Medium . . . . .	8
2. The Excess Electric Dipole $sp$ Radiation in the Far Field. . . . .	14
3. Schematic Sketches of the Atomic Arrangements in (a) A Crystalline Solid, (b) An Amorphous Solid, and (c) A Gas. . . . .	17
4. Schematic Two-dimensional Representation of the Structure of (a) A Hypothetical Crystalline Compound $A_2O_3$ and (b) The Zachariasen Model for the Glassy Form of the Same Compound. . .	17
5. Positions of the Lithium Atoms and the Niobium Atoms with Respect to the Oxygen Octahedra of Lithium Niobate. . . . .	25
6. Schematic of Rayleigh-Brillouin Scattering Apparatus . . . . .	38
7. Top View of the Scattering Geometry and the Wavevector Relations for the Glass Sample . .	42
8. Top View of the Scattering Geometry and the Wavevector Relations for the Lithium Niobate Sample. . . . .	43
9. Top View of the Scattering Geometry and the Wavevector Relations for the RADP Sample. . .	44
10. Arrangement for Measuring the Angle Between the Two Faces of the Sample . . . . .	45
11. Arrangements for Measuring the Refractive Index of the Sample by Determining the Minimum Deviation Angle $D$ . . . . .	46
12. The Collecting Angle. . . . .	50



Figure	Page
13. Procedure for Determining the Primary Quantities in the Brillouin Spectrum. . . . .	51
14. Brillouin Spectra of Fused Quartz . . . . .	61
15. Brillouin Spectra of ZBL AN Fluoride Glass . . . . .	62
16. Brillouin Spectra of BZL Fluoride Glass . . . . .	63
17. The Configurations of Measuring Brillouin Intensities with Changing Light Path $x$ Inside a Sample . . . . .	64
18. Longitudinal Brillouin Intensity $I_L$ Versus the Light Traveled Distance $L$ Inside the Sample . . . . .	65
19. The [100] Phonon Spectra of Pure $\text{LiNbO}_3$ . . . . .	71
20. The [100] Phonon Spectra of 0.2% $\text{Fe}^{+3}$ Doped $\text{LiNbO}_3$ . . . . .	72
21. The $35^\circ$ Y-cut Configuration of Lithium Niobate for Device Applications . . . . .	75
22. The [110] Phonon Spectra of $\text{Rb}_{1-x}(\text{NH}_4)_x\text{H}_2\text{PO}_4$ with Different $x$ ( $\lambda=5145\text{\AA}$ ). . . . .	80
23. The Elastic Constants Versus Ammonium Concentration $x$ . . . . .	81
24. The Structure and Bonding in RADP . . . . .	82
25. The Photoelastic Constant $P_{31}$ Versus Ammonium Concentration $x$ . . . . .	83
26. The Transmission and the Solid Angle Correction Factor. . . . .	96
27. The Relation Among the Wavevectors for the Case in Which the Incident Light is Polarized Along the C-axis While the Scattered Light is Polarized Perpendicular to the C-axis. . . . .	101

## CHAPTER I

### INTRODUCTION

#### A Historical Survey of Brillouin Scattering

In 1922, Brillouin predicted that there would be components in the spectrum of light scattered by liquids and solids whose frequency would be shifted from that of the incident light via interactions with thermally excited sound waves in the scattering medium<sup>[1]</sup>. This effect was first observed in 1930 by Gross<sup>[2]</sup>, and was subsequently studied in a large number of liquids and crystals. The experiments were traditionally performed using a mercury discharge lamp as the source of exciting light. The resultant low signal levels and limited resolution severely limited the use of Brillouin scattering for high-precision spectroscopy.

The advent of CW gas lasers have revolutionized the experimental techniques. The first laser-excited Brillouin-scattering experiments were reported simultaneously by two groups in 1964. Benedek et al. utilized a grating spectrometer for analysis of the scattered light<sup>[3]</sup>. Chiao and Stoicheff employed a pressure-swept Fabry-Perot interferometer<sup>[4]</sup>. The

sensitivity of this apparatus is greatly enhanced by the use of a small-cathode photomultiplier tube together with photon counting pulse-height analysis equipment. Brillouin scattering has become a powerful experimental technique and a active research branch in laser spectroscopy.

### The Work Reported in This Thesis

There are four kinds of observables in the Brillouin spectrum: the Brillouin shifts, peak intensities, peak shapes and background intensity. The first three of these are related to the physical properties of the materials: elastic constants, photoelastic constants, density, index of refraction and the phonon relaxation time.

This thesis reports the Brillouin scattering experiments conducted on three kind of materials:

- A. fluoride glasses.
- B. lithium niobate.
- C. RADP.

Fluoride glasses are potentially useful for the development of very long optical communication lines in the infrared range. The elastic constants, photoelastic constants and the Rayleigh scattering losses of two different fluoride samples were measured using Brillouin scattering and compared with the results of fused quartz. The weak TA peaks were successfully recorded and the small values of the  $P_{44}$  photoelastic coefficient were determined.

Lithium Niobate ( $\text{LiNbO}_3$ ) is centrally important in integrated and guided-wave optics. It is characterized by large pyroelectric, piezoelectric, electro-optic, and photoelastic coefficients. Brillouin scattering measurements were performed on a pure sample and a 0.2%  $\text{Fe}^{+3}$  doped sample. The elastic constants  $C_{11}$  and  $C_{66}$ , the photoelastic coefficients  $P_{31}$  and  $P_{41}$  were measured using Brillouin scattering. To compare the usefulness of acousto-optic materials for device applications several figures of merit were calculated. These values obtained by using Brillouin spectroscopy are in good agreement with the reported values by using other techniques<sup>[5]</sup>.

Rubidium Dihydrogen Phosphate (RDP) and Ammonium Dihydrogen Phosphate (ADP) are isomorphs of KDP. The mixed crystals of ferroelectric  $\text{RbH}_2\text{PO}_4$  (RDP) and anti-ferroelectric  $\text{NH}_4\text{H}_2\text{PO}_4$  (ADP) constitute a new family of solid solutions called RADP:  $\text{Rb}_{1-x}(\text{NH}_4)_x\text{H}_2\text{PO}_4$ . The effective elastic constant of LA[110] mode and elastic constant  $C_{44}$ , the photoelastic coefficients  $P_{31}$ ,  $P_{4,23}$ ,  $P_{4,32}$  and  $P_{66}$  were measured as a function of the ammonium concentration,  $x$ .

#### A Review of Previous Work

The use of optical scattering to study amorphous solids (glass) dated from the work of Lord Rayleigh in 1919<sup>[6]</sup> and continues to the present day. During the 1970's, a considerable number of optical measurements were

performed on silicate glasses<sup>[7]</sup>.

Increasing attention has been recently paid to glasses based on heavy metal fluorides for their potential usefulness in the development of very long optical communication lines in the near infrared range. The molecular structure, morphology, and optical behavior of fluoride glasses are at variance with the oxide-based glasses. In 1985, J.Schroeder et al. using Rayleigh and Brillouin light scattering, studied two specific classes of fluoride glasses - the fluorozirconates and the fluorohafnates<sup>[8]</sup>. This study resulted in valuable information for understanding the possible scattering mechanisms in these glasses. In addition to obtaining the elastic and photoelastic (Pockels) coefficients, the authors also determined the Rayleigh scattering losses for several different samples. The results indicated that some of these glasses exhibit less Rayleigh scattering than fused quartz. In 1987, I.A.Grishin et al. using Brillouin scattering measured the elastic and photoelastic constants of a fluorozirconate glass sample and calculated the Rayleigh losses. But they were unable to record the transverse components in the Brillouin scattering spectrum of this glass<sup>[9]</sup>.

Lithium niobate ( $\text{LiNbO}_3$ ) is centrally important in integrated and guided-wave optics. It is a man-made dielectric material that does not exist in nature. It was first discovered to be ferroelectric in 1949<sup>[10]</sup>. Lithium

niobate was synthesized in single crystal form and investigated in detail at Bell Laboratories. This resulted in an important series of five papers published in 1966 about the structure and properties of the material<sup>[11-15]</sup>. R.J. O'Brien et al. (1969) reported on Brillouin scattering studying in a single crystal of  $\text{LiNbO}_3$ . The elastic constants and piezoelectric constants were determined and corrections to the former values were made by considering the contribution of the internal fields<sup>[16]</sup>. Many experiments have been done on lithium niobate and the reported elastic and photoelastic constants were usually in a good agreement, although large discrepancies were found in some of these reported values<sup>[17]</sup>.

RADP is a new family of solid solutions consisting of the mixed crystals of ferroelectric RDP and anti-ferroelectric ADP. Great interest in these materials has developed since the first publication in 1982<sup>[18]</sup>. Various experiments have been performed on these structural glasses. Recently, some extensive temperature dependent Brillouin scattering experiments have been done for the concentrations  $x = 0.25$ ,  $x = 0.35$ , and  $x = 0.72$  <sup>[19,20]</sup>. A. Bouchalchka recently studied the Brillouin shifts of the LA[110] phonon as a function of temperature. He found that this Brillouin shift undergoes some softening around 100K and begins to harden below 50K due to both a linear and a quadratic coupling of the LA[110] acoustic mode with the polarization fluctuations in the RADP material<sup>[21]</sup>.

## CHAPTER II

### THEORY

#### Thermal Agitation and Brillouin Scattering

We consider a plane monochromatic light wave:

$$\vec{E}(r, t) = \vec{E}_0 \exp[i\vec{K} \cdot \vec{r} - \omega t] \quad (1)$$

incident on a volume  $V$  filled with a perfect homogeneous transparent material. In our case the wavelength of incident light  $\lambda$  is much larger than the interatomic spacing  $a_i$ , i.e.  $\lambda \gg a_i$  ( $i = 1, 2, 3$ ). The Bragg diffraction condition in crystal is:

$$\Delta\vec{K} = \vec{G} \quad (2)$$

$\vec{G}$  is any reciprocal lattice vector, defined:

$$\vec{G} = h \vec{b}_1 + k \vec{b}_2 + l \vec{b}_3 \quad (3)$$

where  $h, k, l$  are integers and  $\vec{b}_i$  ( $i = 1, 2, 3$ ) are reciprocal base vectors:

$$\vec{b}_1 = \frac{2\pi \vec{a}_2 \times \vec{a}_3}{\vec{a}_1 \cdot \vec{a}_2 \times \vec{a}_3}; \quad \vec{b}_2 = \frac{2\pi \vec{a}_3 \times \vec{a}_1}{\vec{a}_1 \cdot \vec{a}_2 \times \vec{a}_3}; \quad \vec{b}_3 = \frac{2\pi \vec{a}_1 \times \vec{a}_2}{\vec{a}_1 \cdot \vec{a}_2 \times \vec{a}_3}. \quad (4)$$

For light scattering in which the relative frequency change  $\Delta\omega/\omega = \Delta K/K \ll 1$ , the relation between the magnitude of wavevector change and scattering angle can be expressed:

$$|\Delta K| = 2 n |K_0| \text{SIN}(\theta/2) = 2n \frac{2\pi}{\lambda_0} \text{SIN}(\theta/2). \quad (5)$$

where  $n$  is the refractive index of medium;  $\lambda_0$  is the light wavelength in free space;  $\theta$  is the scattering angle. In our case,  $\frac{2n}{\lambda_0} \ll b_i$ , ( $i = 1, 2, 3$ ), the Bragg condition cannot be satisfied except when both  $\Delta K$  and  $\theta$  equal zero. Therefore, in a perfect homogeneous medium all directions other than the forward direction, will result in the scattered waves cancelling. The light scattering is due to the inhomogeneity of the medium which contains certain grating patterns satisfying the Bragg diffraction condition in a given direction (Fig.1).

Let us consider the dielectric inhomogeneties associated with the thermal agitation of the medium. For our case  $\lambda \gg a_i$  ( $i = 1, 2, 3$ ), we treat the medium as a uniform continuum. The displacement relative to equilibrium position is a function of position and time. It can be expressed as the superposition of the grating components in  $(\vec{q}, \Omega)$  domain.

$$u(\vec{r}, t) = \sum_{\vec{q}, \Omega} u(\vec{q}, \Omega) e^{i(\vec{q} \cdot \vec{r} - \Omega t)} \quad (6)$$

where,  $\vec{q}$  is the complex wave vector:  $\vec{q} = \vec{q}_1 + i \vec{q}_2$ .

$\Omega$  is the complex frequency:  $\Omega = \Omega_1 + i \Omega_2$ .

The general form (6) contains both propagating and non-propagating components. The non-propagating inhomogeneity causes elastic scattering called Rayleigh scattering. The propagating components cause inelastic scattering due to the Doppler shifting in frequency of the



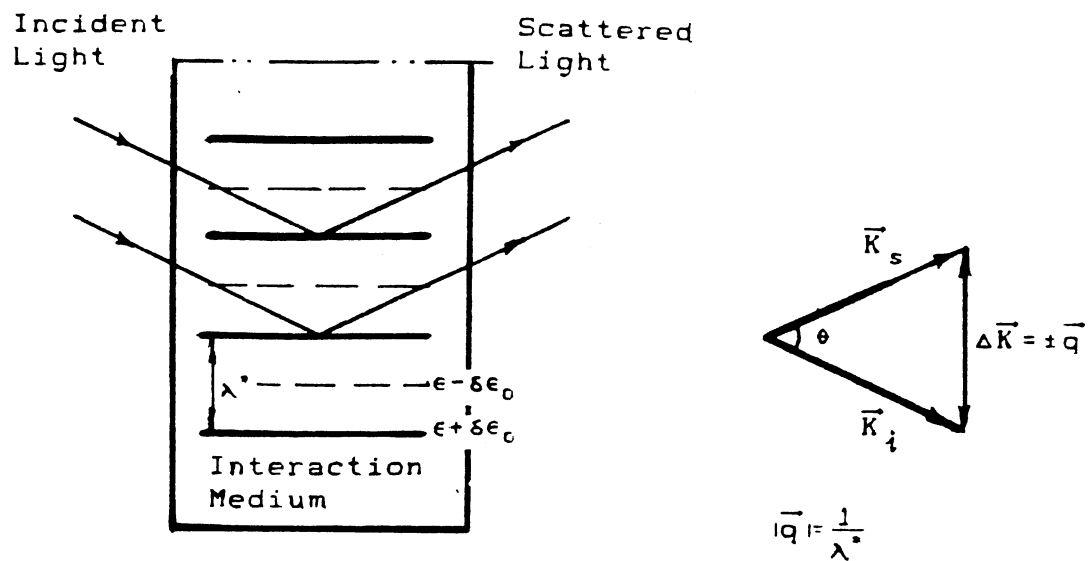


Figure 1. Light Scattered by Inhomogeneous Patterns in the Medium.

The Non-propagating Inhomogeneity Causes Elastic Scattering. The Propagating Components Cause Inelastic Scattering.

scattered light relative to the incident light.

Brillouin Shifts and Elastic Constants  
of Material.

Brillouin scattering is the scattering of light by acoustic waves in a medium. Since light scattering only interacts with acoustic modes whose wavelength is comparable to the wavelength of the light (Bragg condition), the wavevector of the active mode satisfies

$|q| \ll \frac{\pi}{a_1}$ . In this central region of the dispersion

curve, we have<sup>[22]</sup>:

$$\Omega = q v \quad (7)$$

where  $\Omega$  is the acoustic frequency and  $v$  is the sound velocity. The conservation of energy and momentum between the photons and phonons requires:

$$\omega_s = \omega_0 \pm \Omega \quad (8a)$$

$$\vec{K}_s = \vec{K}_0 \pm \vec{q} \quad (8b)$$

where  $\Omega$  is the frequency and  $\vec{q}$  is the wavevector of phonon. The (-) sign represents the Stokes event and the (+) sign represents the Anti-Stokes event.

Because the velocity of the acoustic wave is much smaller than the velocity of light, the frequency of the phonon is much less than the frequency of light, i.e.,  $\Omega \ll \omega_s$ . Therefore, using the conservation equations given above, a light scattering experiment selects those modes for which

$$|q| = 2 n |K_0| \sin \frac{\theta}{2} \quad (9)$$

Combining (8) and (9):

$$v = \frac{\Omega}{q} = \frac{\Omega}{2 n |K_0| \text{SIN}(\frac{\theta}{2})}$$

$$v = \frac{\lambda_0 c \Delta\omega_b}{2 n \text{SIN}(\frac{\theta}{2})} \quad (10)$$

where  $\Omega = c \Delta\omega_b$ ,  $\Delta\omega_b$  is the Brillouin shift in  $\text{cm}^{-1}$  unit.

We analyze the lattice dynamics using the familiar harmonic approximation. The stress is:

$$S_{ik} = C_{iklm} \frac{\partial u_m}{\partial X_l} \quad (11)$$

where  $C_{iklm}$  is the elastic stiffness tensor. The equation of motion is:

$$\rho \frac{\partial^2 u_i}{\partial t^2} = \frac{\partial S_{ik}}{\partial X_k} = C_{iklm} \frac{\partial^2 u_m}{\partial X_k \partial X_l} \quad (12)$$

$$\text{Assume: } u_m = u_m^0 e^{i(\vec{q}\vec{r} - \Omega t)} \quad (13)$$

Substitute (13) into (12),

$$\rho \Omega^2 u_i^0 = C_{iklm} q_k q_l u_m^0 \quad (14)$$

or,

$$\left[ C_{iklm} \hat{q}_k \hat{q}_l - \rho v^2 s_{im} \right] u_m^0 = 0 \quad (15)$$

for the long wavelength acoustic modes  $\Omega = v q$ . Thus,

(15) has non-trivial solutions only if the secular determinant vanishes:

$$\left| C_{iklm} \hat{q}_k \hat{q}_l - \rho v^2 s_{im} \right| = 0 \quad (16)$$

where  $\hat{q}_k = \frac{q_k}{|q|}$  is the k-component of unit vector  $\hat{q}$ .

Finding the phonon velocity of the material from the Brillouin spectrum through eq. (10), eq. (16) can be used to determine the elastic constants in a high symmetry direction. The elastic constants so determined are indicative of the properties of the material at frequency

$\Omega_1 = v_1 q$  which is around  $10^9 - 10^{10}$  Hz. Brillouin scattering experiments therefore complement ultrasonic and static elastic constant measurements.

Brillouin Scattering Cross Section and Photoelastic Constants of the Material.

The scattering cross section can be determined by calculating the excess polarization radiation in the far field. The excess polarization is caused by the interaction between the incident light field and the dielectric inhomogeneity. The dielectric inhomogeneities are associated with the thermal agitation of the medium. The observed change in the refractive index of the solid under strain arises from a combination of the following three effects: 1) changes in the local Coulomb field due to a shift in positions of charge centers, 2) changes in the local Lorentz-Lorenz cavity field and 3) changes in the polarizability of the constituent ions or atoms<sup>[23]</sup>. The coupling between the dielectric constant fluctuation

$\delta(\epsilon^{-1})_{\alpha\beta}$  and the displacement gradient  $\frac{\partial u_\nu}{\partial X_\eta}$  can be

expressed as:

$$\delta(\epsilon^{-1})_{\alpha\beta} = P_{\alpha\beta,\nu\eta} \frac{\partial u_\nu}{\partial X_\eta} \quad (17)$$

or:

$$\delta\epsilon_{\alpha\beta} = -\epsilon_{\alpha\alpha} \epsilon_{\beta\beta} P_{\alpha\beta,\nu\eta} \frac{\partial u_\nu}{\partial X_\eta} \quad (18)$$

where  $P_{\alpha\beta,\nu\eta}$  is the photoelastic tensor. Because the gradient  $\frac{\partial u_\nu}{\partial X_\eta}$  and the dielectric constant  $\epsilon_{\alpha\beta}$  are second rank tensors, the photoelastic constant  $P_{\alpha\beta,\nu\eta}$  is a fourth rank tensor which has a total of 81 elements. The fact that  $\delta\epsilon_{\alpha\beta}$  is symmetrical in  $\alpha$  and  $\beta$  and  $\frac{\partial u_\nu}{\partial X_\eta}$  is symmetrical in  $\nu$  and  $\eta$  (in isotropic materials) leaves 36 independent components of  $P_{\alpha\beta,\nu\eta}$ . Therefore, the 4 index notation can be replaced by a 2 index notation as follows<sup>[24]</sup>:

11  $\rightarrow$  1; 22  $\rightarrow$  2; 33  $\rightarrow$  3; 23, 32  $\rightarrow$  4; 31, 13  $\rightarrow$  5;  
12, 21  $\rightarrow$  6 .

In this new notation Eq. (18) becomes:

$$\delta\epsilon_m = -\epsilon_\alpha \epsilon_\beta P_{mn} \left( \frac{\partial u}{\partial X} \right)_n \quad (m, n = 1, 2, \dots, 6) \quad (19)$$

Of course, the symmetry properties of a material will reduce the number of independent photoelastic constants even further.

We also analyze the dielectric fluctuation in the  $(\vec{q}, \Omega)$  domain. It is the superposition of different inhomogeneous patterns in the medium:

$$\delta\epsilon(\vec{r}, t) = \sum_{\vec{q}, \Omega} \delta\epsilon(\vec{q}, \Omega) e^{i(\vec{q} \cdot \vec{r} - \Omega t)} \quad (20)$$

The coupling of the electric field (incident light) with the dielectric inhomogeneous patterns creates the excess electric dipole moment (excess polarization) which radiates the scattering field. The polarization is given by:

$$\vec{p} = \chi_e \vec{E} \quad (21)$$

and the relation between the electric susceptibility  $\chi_e$  and dielectric constant  $\epsilon$  is:

$$\epsilon = 1 + 4\pi\chi_e \quad (22)$$

so, the excess dipole moment  $\delta\vec{p}$  is:

$$\delta p_\alpha = \frac{1}{4\pi} \delta\epsilon_{\alpha\beta} E_{0,\beta} \quad (23)$$

Consider a small volume element. Set the origin of the spherical coordinate at the position of the element and let the polar axis be along the direction of the dipole (Fig.2). If  $\delta\vec{p} = \delta p_0 e^{i\omega_s t} \hat{z}_0$ , the scattered light radiated by  $\delta\vec{p}$  in far field will be<sup>[25]</sup>:

$$\vec{E}_s(\vec{r}, t) = \delta\ddot{p} \frac{1}{c^2 r} e^{i\vec{k}\vec{r}} \text{SIN}\theta \hat{e}_\theta \quad (24)$$

where  $\delta\ddot{p}$  is the second order derivative of  $\delta p$  with respect to time  $t$  and  $\theta$  is the angle between  $\delta\vec{p}$  and  $\vec{r}$ . Now we concentrate on a single normal mode of the system and choose the polarization for the incident and scattered light. Use (23) and substitute:

$$\delta\epsilon_m(q, \Omega) = -\epsilon_\alpha \epsilon_\beta P_{mn}(qu)_n e^{i(\vec{q}\vec{r} - \Omega t)} \quad (25)$$

$$E_{0,\beta} = E_0 e^{i(\vec{k}_0\vec{r} - \omega_0 t)} \quad (26)$$

and integrate over scattering volume  $V$ , the scattered field will be:

$$E_s = \frac{\omega_s^2}{4\pi c^2 r} \text{SIN}\theta \epsilon_\alpha \epsilon_\beta P_{mn}(qu)_n E_0 V e^{i(\vec{k}_s\vec{r} - \omega_s t)} \quad (27)$$

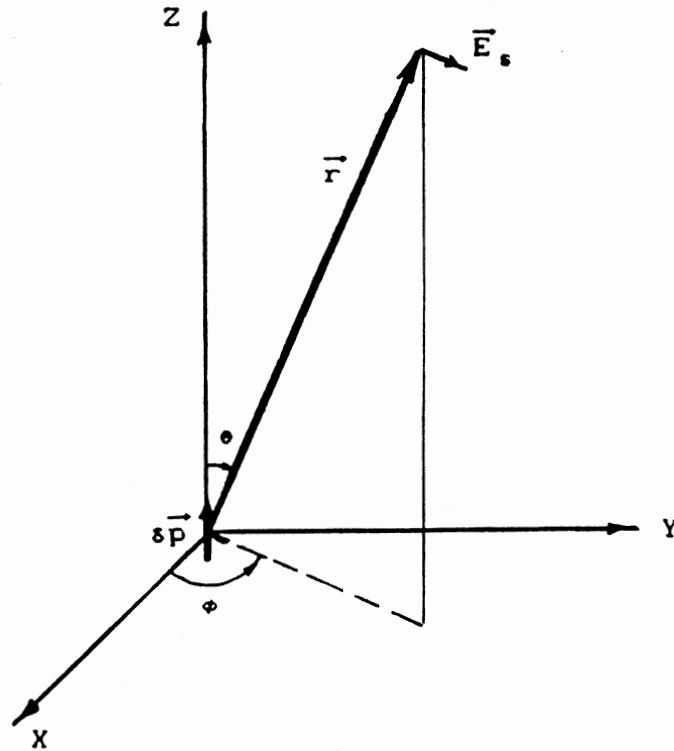


Figure 2. The Excess Electric Dipole  $\vec{sP}$  Radiation in Far Field.

$$\delta\vec{p} = \delta p_0 e^{i\omega_s t} \hat{z}_0$$

$$\vec{E}_s(\vec{r}, t) = \delta\ddot{p} \frac{1}{c^2 r} e^{i\vec{k}\vec{r}} \text{SIN}\theta \hat{e}_0$$

where  $\omega_s = \omega_0 \pm \Omega$

$$\vec{k}_s = \vec{k}_0 \pm \vec{q}$$

The scattering cross section is defined as the flux scattered into a unit solid angle per unit volume per unit incident intensity. It can be calculated using the following:

$$\begin{aligned} \frac{d\sigma}{d\Omega} &= \frac{r^2 I_s}{V I_0} = \frac{r^2}{V} \frac{|E_s|^2 (c/n_0)}{|E_0|^2 (c/n_s)} \\ &= \frac{\omega_s^4 V}{16 \pi^2 c^4} [\text{SIN}\theta \epsilon_\alpha \epsilon_\beta P_{mn}(qu)_n]^2 \left(\frac{n_s}{n_0}\right) \end{aligned} \quad (28)$$

Consider the following facts:

(1). The multiplication of 6 X 6 Pockel's tensor  $P_{mn}$  and six-components (6 X 1) displacement gradient  $(qu)_n$  gives 6-components which can be converted to 3 X 3 matrix form.

(2). For the long wavelength acoustic phonon  $h\Omega \ll KT$ , in classical thermodynamic equilibrium each elastic vibration mode shares 1/2 KT of kinetic and potential energy. Therefore we can relate the elastic deformation to the thermal energy KT and elastic constant. For each mode

$$C_{eff} \langle (qu)^2 \rangle V = \rho v^2 \langle (qu)^2 \rangle V = \frac{KT}{2} \quad (29)$$

Then the term  $[\text{SIN}\theta \epsilon_\alpha \epsilon_\beta P_{mn}(qu)_n]^2$  can be converted to

$$\frac{KT}{2 \rho v^2 V} (\hat{e}_s T \hat{e}_0)^2 \quad (30)$$

where T is 3 X 3 Brillouin scattering tensor, the elements of T are  $\epsilon_\alpha \epsilon_\beta$  times the photoelastic constants  $P_{mn}$

(Pockel's coefficients).  $\hat{e}_s$  and  $\hat{e}_0$  are the unit polarization vectors of incident and scattered light,



respectively.

Finally, the Brillouin scattering cross-section (also called the Rayleigh ratio) of the  $j$ th acoustic mode is given by<sup>[26]</sup>:

$$\begin{aligned}
 R^j &= \frac{KT \omega_s^4}{32 \pi^2 c^4 \rho v_j^2} [\hat{e}_s^T J^j \hat{e}_o]^2 (n_s/n_o) \\
 &= \frac{KT \pi^2}{2 \lambda_s^4 \rho v_j^2} [\hat{e}_s^T J^j \hat{e}_o]^2 (n_s/n_o) \quad (31)
 \end{aligned}$$

Thus the choice of polarization for the incident and scattered light selects specific acoustic modes. The Brillouin spectrum is therefore related with two sets of material constants: the elastic constants  $C_{ijkl}$  which determine the positions of the Brillouin components, while the Pockel's coefficients  $P_{ijkl}$  determine the intensities.

#### Rayleigh and Brillouin Scattering in Glass

Glass is formed by supercooling the melt past its freezing point through its "glass transition" range. The principal structural order present is imposed by the approximately constant separation of nearest-neighbor atoms or molecules (Fig.3,4).

The Rayleigh-Brillouin spectrum allows the separation of two basic processes causing light scattering: The scattering by propagating fluctuations in the dielectric constant (Brillouin scattering) and the scattering by nonpropagating diffusive fluctuations (Rayleigh scattering).

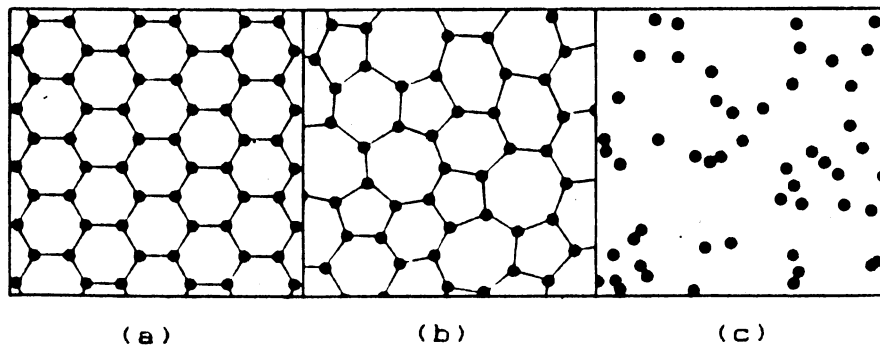


Figure 3. Schematic Sketches of the Atomic Arrangements in (a) A Crystalline Solid, (b) An Amorphous Solid, and (c) A Gas. [27]

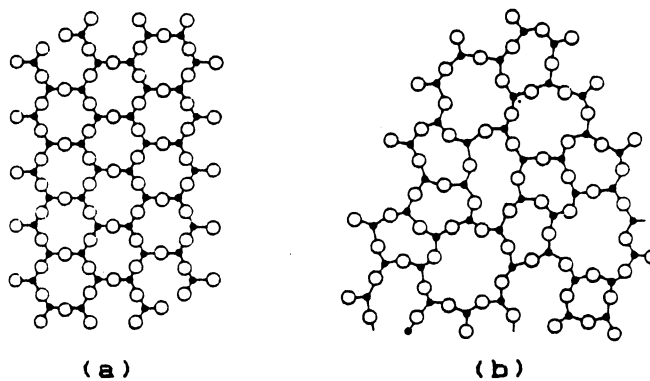


Figure 4. Schematic Two-dimensional Representation of the Structure of (a) A Hypothetical Crystalline Compound  $A_2O_3$  and (b) The Zachariasen Model for the Glassy Form of the Same Compound. [28]

The rate of cooling during glass formation is such that the equilibrium structure of the melt can no longer change. The density (nonpropagating part) and composition fluctuation are literally frozen into the newly formed solid. The structural relaxation time is so long that upon lowering the temperature no further structural rearrangement is possible. The density fluctuation is effectively frozen at a viscosity of about  $10^{13.5}$  P, while composition fluctuations are thermally arrested at a viscosity of about  $10^7$ - $10^8$  P. Hence one can assume that the magnitude of these structural fluctuations are characterized by two "fictive temperatures":  $T_f^d$  and  $T_f^c$ , respectively. The  $T_f^d$  is approximately equal to the glass transition temperature  $T_g$  while  $T_f^c$  is higher. The Rayleigh scattering intensity can be determined by using thermodynamic fluctuation theory at these "fictive temperatures".

However, the Brillouin intensity comes only from lattice contributions, since structural contributions are inaccessible due to their long relaxation times. In the low frequency, long wavelength limit, the precise arrangement of atoms is of little consequence and the amorphous solid appears isotropic and acts as an elastic medium. The vibrational excitations can properly be described as acoustic phonons<sup>[29]</sup>. Consequently, the term describing the vibrational modes (phonons) of the 'random' glass lattice need not be altered since these

phonon modes are in equilibrium at the lattice temperature  $T$ .

For Multicomponent Liquids the  $k$ th spatial Fourier component of the fluctuation in the dielectric constant is [7]:

$$\begin{aligned} \langle \delta \epsilon_k^2 \rangle &= \left( \frac{\partial \epsilon}{\partial \rho} \right)_{T,c}^2 \left( \frac{\partial \rho}{\partial S} \right)_{P,c}^2 \langle \delta S_{red,k}^2 \rangle + \left( \frac{\partial \epsilon}{\partial \rho} \right)_{T,c}^2 \left( \frac{\partial \rho}{\partial P} \right)_{s,c}^2 \langle \delta P_k^2 \rangle + \\ &\sum_{j=1}^{n-1} \sum_{l=1}^{n-1} \left( \frac{\partial \epsilon}{\partial C_j} \right)_{T,P,c} \left( \frac{\partial \epsilon}{\partial C_l} \right)_{T,P,c} \langle (\delta C_j \delta C_l)_k \rangle \end{aligned} \quad (32)$$

where  $\delta S_{red}$  is the reduced entropy fluctuation,  $\delta P$  is the pressure fluctuation,  $\delta C_l$  is the concentration fluctuation of the  $l$ th component. The brackets  $\langle \rangle$  denote the average over an equilibrium ensemble. The pressure fluctuation can be identified to a good approximation with sound waves which cause Brillouin doublets. Both entropy fluctuations and concentration fluctuations may be identified with heat conduction, thermal diffusion, and mass diffusion. All of these are nonpropagating modes which result in Rayleigh scattering.

Using thermodynamic fluctuation theory to determine the mean square fluctuations of the thermodynamic quantities and inserting the "fictive temperatures" for the nonpropagating part in form (32), Schroeder extended the above theory to glass systems and derived the formulas

of the Landau-Placzek ratio which is defined as the ratio of the intensities of the central components  $I_R$  to the total Brillouin components  $2I_b$  for the glass. The density fluctuation part of the Landau-Placzek ratio takes the form

$$R_{LP}(\rho) = \frac{T_f^d}{T} \left[ \frac{K_{T,0}(T_f^d) - (\rho v_{L,\omega}^2)^{-1}}{(\rho v_{L,\omega}^2)^{-1}} \right] (\rho \frac{\partial \epsilon}{\partial \rho})_{T_f}^2 (\rho \frac{\partial \epsilon}{\partial \rho})_{T_f}^{-2} \quad (33a)$$

where  $K_{T,0}$  denotes the equilibrium isothermal compressibility. The concentration fluctuation part of the Landau-Placzek ratio part becomes

$$R_{LP}(c) = \frac{T_f^c \sum_{i,j=1}^{n-1} (\frac{\partial \epsilon}{\partial c_i})_{T,P,c} (\frac{\partial \epsilon}{\partial c_j})_{T,P,c} (\frac{\partial \tilde{\mu}}{\partial c_j})_{T,P,c}^{-1}}{T [\rho (\frac{\partial \epsilon}{\partial \rho})]_{T,c}^2 (v_{L,\omega}^2)^{-1}} \quad (33b)$$

where  $\tilde{\mu} = \mu_j - \mu_n$  and  $\mu_j$  is the chemical potential of  $j$ th component. The Landau-Placzek ratio is the sum of the two parts

$$R_{LP} = R_{LP}(\rho) + R_{LP}(c) \quad (34)$$

### Elastic Constants of Glass

Elasticity is a centrosymmetric property. This means that if the reference axes are transformed by the operation of a center of symmetry the  $C_{ijkl}$  components

remain unaltered. From this, for isotropic medium, the form of the elastic constant  $(C_{mn})$  matrix is given by<sup>[24]</sup>:

$$(C_{mn}) = \begin{pmatrix} C_{11} & C_{12} & C_{12} & 0 & 0 & 0 \\ C_{12} & C_{11} & C_{12} & 0 & 0 & 0 \\ C_{12} & C_{12} & C_{11} & 0 & 0 & 0 \\ 0 & 0 & 0 & \frac{1}{2}(C_{11}-C_{12}) & 0 & 0 \\ 0 & 0 & 0 & 0 & \frac{1}{2}(C_{11}-C_{12}) & 0 \\ 0 & 0 & 0 & 0 & 0 & \frac{1}{2}(C_{11}-C_{12}) \end{pmatrix} \quad (35)$$

where  $C_{44} = \frac{1}{2}(C_{11} - C_{12})$ . Note there are only two independent elements in the elastic constant matrix. Using (35) and setting  $\hat{q} = [1, 0, 0]$ , equation (15) results in the following eigenvalues and eigenvectors,

$$(\rho v^2)_1 = C_{11}, \quad \hat{u} = (1, 0, 0)$$

$$(\rho v^2)_2 = C_{44}, \quad \hat{u} = (0, 1, 0) \text{ and } (0, 0, 1)$$

The first solution corresponds to the longitudinal acoustic mode and the second solution corresponds to the two degenerate transverse acoustic modes.

### Brillouin Scattering Cross Section of Glass

The form of the photoelastic matrix  $(P_{mn})$  are obtained in a similar way as the elastic constant matrix. For isotropic media,  $(P_{mn})$  is given by<sup>[24]</sup>:

$$(P_{mn}) = \begin{pmatrix} P_{11} & P_{12} & P_{12} & 0 & 0 & 0 \\ P_{12} & P_{11} & P_{12} & 0 & 0 & 0 \\ P_{12} & P_{12} & P_{11} & 0 & 0 & 0 \\ 0 & 0 & 0 & \frac{1}{2}(P_{11}-P_{12}) & 0 & 0 \\ 0 & 0 & 0 & 0 & \frac{1}{2}(P_{11}-P_{12}) & 0 \\ 0 & 0 & 0 & 0 & 0 & \frac{1}{2}(P_{11}-P_{12}) \end{pmatrix} \quad (36)$$

where  $P_{44} = \frac{1}{2}(P_{11} - P_{12})$ . There are only two independent matrix elements for the isotropic material. The Brillouin scattering matrix is determined by

$$T_m = \epsilon_\alpha \epsilon_\beta P_{mn} x_n = \epsilon_0^2 P_{mn} x_n \quad (37)$$

where  $x_n$  is the normalized strain matrix:

$$x_1 = (\hat{q}_x \hat{u}_x) \quad (38a)$$

$$x_2 = (\hat{q}_y \hat{u}_y) \quad (38b)$$

$$x_3 = (\hat{q}_z \hat{u}_z) \quad (38c)$$

$$x_4 = (\hat{q}_y \hat{u}_z + \hat{q}_z \hat{u}_y) \quad (38d)$$

$$x_5 = (\hat{q}_x \hat{u}_z + \hat{q}_z \hat{u}_x) \quad (38e)$$

$$x_6 = (\hat{q}_x \hat{u}_y + \hat{q}_y \hat{u}_x) \quad (38f)$$

where  $\hat{q}$  is the unit vector indicating the propagation direction of the acoustic wave and  $\hat{u}$  is the unit vector indicating the local displacement direction. Choosing  $\hat{q} = [1, 0, 0]$  for the phonon propagation direction, we can derive three Brillouin scattering tensors  $T^L$ ,  $T^T_1$ , and  $T^T_2$  for one longitudinal mode and two transverse modes respectively. For the longitudinal wave,  $\hat{u} = (1, 0, 0)$ :

$$x_1 = 1, \quad x_2 = x_3 = x_4 = x_5 = x_6 = 0$$

Multiplying  $(P_{mn})$ ,  $(x_n)$  and  $\epsilon_0^2$  yields the Brillouin scattering matrix:

$$(T_M) = \epsilon_0^2 ( P_{11}, P_{12}, P_{12}, 0, 0, 0 )$$

Converting to the 3 X 3 matrix form:

$$T^L = \epsilon_0^2 \begin{pmatrix} P_{11} & 0 & 0 \\ 0 & P_{12} & 0 \\ 0 & 0 & P_{12} \end{pmatrix} \quad (39)$$

For the transverse modes  $\hat{u}_1 = (0, 1, 0)$  and  $\hat{u}_2 = (0, 0, 1)$ ,

the Brillouin scattering tensors will be:

$$T^{T_1} = \epsilon_0^2 \begin{pmatrix} 0 & P_{44} & 0 \\ P_{44} & 0 & 0 \\ 0 & 0 & 0 \end{pmatrix} \quad (40)$$

$$T^{T_2} = \epsilon_0^2 \begin{pmatrix} 0 & 0 & P_{44} \\ 0 & 0 & 0 \\ P_{44} & 0 & 0 \end{pmatrix} \quad (41)$$

Using a right angle scattering configuration and choosing the polarization for the incident and scattered light, we get the Rayleigh ratio for both LA and TA peaks:

$$\begin{aligned} R^L(VV) &= \frac{KT \omega_s^4}{32 \pi^2 c^4 \rho v_L^2} \epsilon_0^4 P_{12}^2 \frac{n_s}{n_0} \\ &\doteq \frac{KT \omega_0^4}{32 \pi^2 c^4 C_{11}} n_0^8 P_{12}^2 \end{aligned} \quad (42)$$



$$R^{T_2(VH)} = \frac{KT \omega_0^4}{32 \pi^2 c^4 C_{44}} \frac{1}{2} n_0^8 P_{44}^2 \quad (43)$$

for  $\hat{q} = [100]$  and the following electric polarizations:

$$\text{Incident vertical (V): } \hat{e}_0 = (0, 0, 1)$$

$$\text{Scattered vertical (V): } \hat{e}_s = (0, 0, 1)$$

$$\text{Scattered horizontal (H): } \hat{e}_s = \frac{1}{\sqrt{2}}(1, 1, 0).$$

### Brillouin Scattering in Lithium Niobate

Lithium Niobate is a ferroelectric material. A ferroelectric can show a spontaneous polarization, but it has the additional property that the polarization can be reversed by applying a sufficiently large electric field. In a strong alternating field it therefore shows hysteresis. Ferroelectrics form a group of crystals of great theoretical interest. The spontaneous polarization and hysteresis which characterize them are accompanied by other special properties. Lithium Niobate has a trigonal crystal structure (3m point group) and is characterized by large pyroelectric, piezoelectric, electro-optic, and photoelastic coefficients. Lithium niobate's structure at temperatures below its ferroelectric Curie temperature (approximately 1210°C) consists of planar sheets of oxygen atoms in a distorted hexagonal close-packed configuration. The octahedral interstices formed in this structure are one-third filled by niobium atoms, and one-third vacant. The charge separation (Fig. 5 )

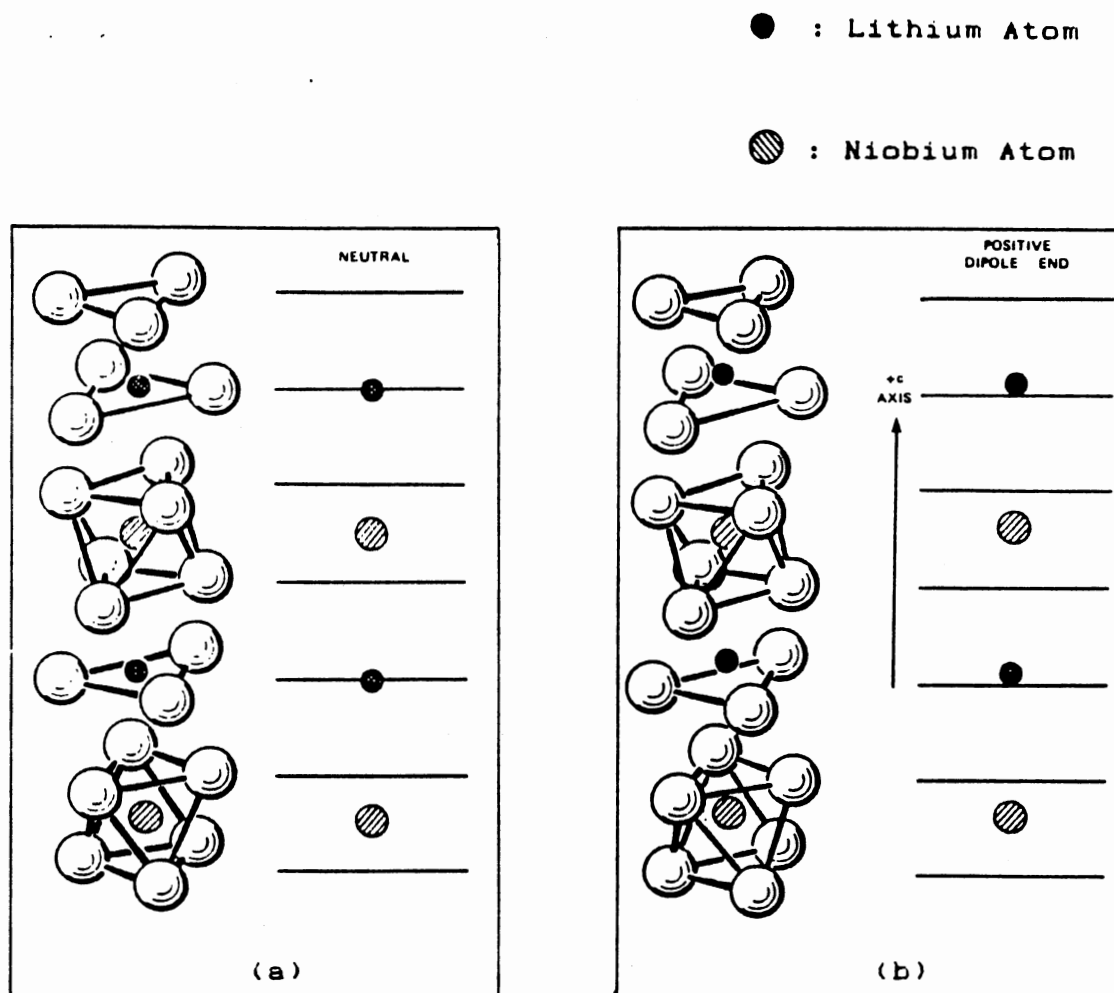


Figure 5. Positions of the Lithium Atoms and the Niobium Atoms with Respect to the Oxygen Octahedra of Lithium Niobate. (a) In the Paraelectric Phase ( $T \geq T_c$ ), and (b) In the Ferroelectric Phase ( $T \leq T_c$ ). [17]

resulting from the shift of ions relative to the oxygen octahedra causes  $\text{LiNbO}_3$  to exhibit spontaneous polarization at temperatures below  $1210^\circ\text{C}$ . Thus,  $\text{LiNbO}_3$  belongs to the broad class of displacement ferroelectrics.

In  $\text{LiNbO}_3$  a second effect may be significant on the effective elastic constants and photoelastic coefficients which we observe. In this case, the applied strain causes an electric field through the piezoelectric effect. This electric field then causes a change in the crystal's refraction index through the linear electro-optic effect, this secondary contribution is inseparable from the primary photoelastic effect. The indirect photoelastic effect cannot be represented as an ordinary tensor but instead must be expressed as a tensor that is dependent on the acoustic wave direction<sup>[30]</sup>.

#### Elastic Constants of Lithium Niobate

The elastic tensor ( $C_{mn}$ ) for  $\text{LiNbO}_3$  has the following form<sup>[24]</sup>:

$$(C_{mn}) = \begin{pmatrix} C_{11} & C_{12} & C_{13} & C_{14} & 0 & 0 \\ C_{12} & C_{11} & C_{13} & -C_{14} & 0 & 0 \\ C_{12} & C_{13} & C_{33} & 0 & 0 & 0 \\ C_{14} & -C_{14} & 0 & C_{44} & 0 & 0 \\ 0 & 0 & 0 & 0 & C_{44} & C_{14} \\ 0 & 0 & 0 & 0 & C_{14} & \frac{1}{2}(C_{11}-C_{12}) \end{pmatrix} \quad (44)$$

and contains six independent coefficients. When determining the values of these coefficients, the contribution of the piezoelectric effect must be taken into account. The supplementary stress components  $\Delta S_{ik}$  as well as a polarization  $\Delta P_i$  are expressed by the relations

$$\Delta S_{ik} = -e_{j,ik} E_j \quad (45a)$$

$$\Delta P_i = e_{i,m1} \frac{\partial u_m}{\partial X_1} \quad (45b)$$

where  $e_{j,ik}$  is the piezoelectric tensor which has the form by symmetry<sup>[24]</sup>:

$$(e_{jn}) = \begin{pmatrix} 0 & 0 & 0 & 0 & e_{15} & -e_{22} \\ -e_{22} & e_{22} & 0 & e_{15} & 0 & 0 \\ e_{31} & e_{31} & e_{33} & 0 & 0 & 0 \end{pmatrix} \quad (46)$$

Thus the piezoelectric effect in lithium niobate can be described by four independent coefficients:  $e_{15}$ ,  $e_{22}$ ,  $e_{31}$ ,  $e_{33}$ . The total stress for adiabatic conditions is:

$$S_{ik} = C_{iklm}^E \frac{\partial u_m}{\partial X_l} - e_{j,ik} E_j \quad (47)$$

where  $C_{iklm}^E$  is the elastic constant tensor for constant electric field. For quasi-static fields in non-magnetic, non-conducting, charge free media, Maxwell's equations are given by

$$\nabla \times \vec{E} = 0 \quad \text{and} \quad \nabla \times \vec{D} = 0 \quad (48)$$

where  $\vec{E}$  is the stress induced internal field, and

$$D_j = e_{j1} E_1 + e_{j,im} \frac{\partial u_m}{\partial X_i} \quad (49)$$

where,  $e_{j,im}$  is the piezoelectric tensor and  $e_{j1}$  is

the dielectric constant tensor.

Simultaneous solutions of eqs. (47), (48), (49), and the equation of motion (12) using plane harmonic waves yields the displacements  $u$  as solutions to the normal mode equation:

$$\rho \omega^2 u_i = C_{iklm}^* u_m q_l q_k \quad (50)$$

where

$$C_{iklm}^* = C_{iklm}^E + \frac{\sum_{j,n} e_{j,ik} e_{n,lm} \hat{q}_j \hat{q}_n}{\sum_{p,n} \epsilon_{pn} \hat{q}_p \hat{q}_n} \quad (51)$$

is the effective elastic constant and the  $\hat{q}$ 's are the direction cosines of the phonon.

Choosing  $\hat{q} = [1, 0, 0]$  and using (44), the secular equation (15) can be solved for the eigenvalue and eigenvector of the longitudinal acoustic wave:

$$(\rho v^2)_1 = C_{11}, \quad \hat{u} = (1, 0, 0) \quad (52)$$

From (51), we have

$$C_{11}^* = C_{11}^E + \frac{e_{11} e_{11}}{\epsilon_{11}} = C_{11}^E \quad (53)$$

Choosing  $\hat{q} = [0, 1, 0]$  and using (44), the secular equation (15) can be solved for the eigenvalue and eigenvector of one transverse acoustic wave:

$$(\rho v^2)_2 = C_{66}, \quad \hat{u} = (1, 0, 0) \quad (54)$$

From (51), we have

$$C_{66}^* = C_{66}^E + \frac{e_{26} e_{26}}{\epsilon_{22}} = C_{66}^E \quad (55)$$

According to (44)

$$C_{12} = C_{11} - 2C_{66} \quad (56)$$

Brillouin Scattering Cross Section of  
Lithium Niobate

In a piezoelectric media, the strain induced electric field as functions of  $u$  are expressed in the following form<sup>[31]</sup>:

$$E_n = -iq_n \frac{\sum_{m,i,j} e_{m,i,j} \hat{q}_i \hat{q}_m u_j}{\sum_{m,n} \epsilon_{mn} \hat{q}_m \hat{q}_n} \quad (57)$$

The electro-optic effect causes a supplementary change in the dielectric constant due to the presence of an electric field

$$\delta(\epsilon^{-1})_{i,j} = r_{ijm} E_m \quad (58)$$

where  $r_{ijm}$  are the zero strain electro-optic coefficients

which have the form<sup>[24]</sup>:

$$(r_{in}) = \begin{pmatrix} 0 & -r_{22} & r_{13} \\ 0 & r_{22} & r_{13} \\ 0 & 0 & r_{33} \\ 0 & r_{42} & 0 \\ r_{42} & 0 & 0 \\ -r_{22} & 0 & 0 \end{pmatrix} \quad (59)$$

There are four independent coefficients in this matrix similar to the piezoelectric tensor. Therefore, the total variation of dielectric constant by the coupled displacement gradient and electric field are expressed as:

$$\delta(\epsilon^{-1})_{ij} = r_{ij,m} E_m + P_{ijkl}^E \frac{\partial u_l}{\partial X_k} \quad (60)$$

where  $P_{ijkl}^E$  is the photoelastic tensor for a constant field. The relationship between the elastic wave and the electric field given by eq. (57) leads to an effective photoelastic constant<sup>[32]</sup>:

$$P_{ijkl}^* = P_{ijkl}^E - \frac{\sum_n r_{ij,n} \hat{q}_n \sum_m \epsilon_{m,kl} \hat{q}_m}{\sum_{m,n} \epsilon_{mn} \hat{q}_m \hat{q}_n} \quad (61)$$

where  $P_{ijkl}^*$  are the effective photoelastic constants.

The form of the photoelastic matrix  $(P_{mn})$  is given<sup>[24]</sup>:

$$(P_{mn}) = \begin{pmatrix} P_{11} & P_{12} & P_{13} & P_{14} & 0 & 0 \\ P_{12} & P_{11} & P_{13} & -P_{14} & 0 & 0 \\ P_{31} & P_{31} & P_{33} & 0 & 0 & 0 \\ P_{41} & -P_{41} & 0 & P_{44} & 0 & 0 \\ 0 & 0 & 0 & 0 & P_{44} & P_{41} \\ 0 & 0 & 0 & 0 & P_{14} & \frac{1}{2}(P_{11} - P_{12}) \end{pmatrix} \quad (62)$$

There are eight independent coefficients which need to be considered. For  $\hat{q} = [1, 0, 0]$  and  $\hat{u} = (1, 0, 0)$ , the Brillouin scattering tensor can be calculated by eq. (37)

$$T^L = \begin{pmatrix} \epsilon_0^2 P_{11} & 0 & 0 \\ 0 & \epsilon_0^2 P_{12} & \epsilon_0 \epsilon_e P_{41} \\ 0 & \epsilon_0 \epsilon_e P_{41} & \epsilon_e^2 P_{31} \end{pmatrix} \quad (63)$$

where  $\epsilon_1 = \epsilon_2 = \epsilon_0$  stands for the ordinary dielectric constant and  $\epsilon_3 = \epsilon_e$  stands for the extraordinary

dielectric constant. For  $\hat{q} = [0, 1, 0]$  and  $\hat{u} = (1, 0, 0)$ , the

Brillouin scattering tensor is:

$$T_1^T = \begin{pmatrix} 0 & \epsilon_0^2(P_{11} - P_{12})/2 & \epsilon_0 \epsilon_e P_{41} \\ \epsilon_0^2(P_{11} - P_{12})/2 & 0 & 0 \\ \epsilon_0 \epsilon_e P_{41} & 0 & 0 \end{pmatrix} \quad (64)$$

Using a right angle scattering configuration and choosing the polarization for the incident and scattered light, we can easily determine the Rayleigh ratios for the

longitudinal wave  $\hat{q} = [100]$  and  $\hat{u} = (100)$ :

$$R^L(VV) = \frac{KT \omega_0^4}{32 \pi^2 c^4 \rho v_L^2} n_e^8 P_{31}^2 \quad (65)$$

$$R_2^L(VH) = \frac{1}{2} \frac{KT \omega_0^4}{32 \pi^2 c^4 \rho v_L^2} n_e^4 n_o^4 P_{41}^2 \frac{n_o}{n_e} \quad (66)$$

with  $\rho v_L^2 = C_{11}$  and the following electric polarizations:

Incident vertical (V):  $\hat{e}_o = (001)$

Scattering vertical (V):  $\hat{e}_s = (001)$

Scattering horizontal (H):  $\hat{e}_s = \frac{1}{\sqrt{2}} (110)$

We measure  $P_{31}$  and  $P_{41}$  photoelastic constants

from the  $[100]$  phonon scattering, from (61):

$$P_{31} = P_{31}^E - \frac{r_{31} e_{11}}{\epsilon_{11}} = P_{31}^E \quad (67)$$

$$P_{41} = P_{41}^E - \frac{r_{41} e_{11}}{\epsilon_{11}} = P_{41}^E \quad (68)$$

The Rayleigh ratio for the transverse wave  $\hat{q} = [010]$  and

$\hat{u} = (100)$  scattering:

$$R_2^T(VH) = \frac{1}{2} \frac{KT \omega_0^4}{32 \pi^2 c^4 \rho v_T^2} n_e^4 n_o^4 P_{41}^2 \frac{n_o}{n_e} \quad (69)$$



with  $\rho v_T^2 = (C_{11} - C_{12})/2$  and the following electric polarizations:

$$\text{Incident vertical (V): } \hat{e}_0 = (0, 0, 1)$$

$$\text{Scattering horizontal (H): } \hat{e}_s = \frac{1}{\sqrt{2}} (1, -1, 0)$$

When we measure photoelastic constant  $P_{41}$  from [010] phonon scattering, according to (61):

$$P_{41} = P_{41}^E - \frac{r_{42} e_{21}}{\epsilon_{22}} \quad (70)$$

Nelson and Lax<sup>[33]</sup> (1971) found that the independent elastic variable relevant to the photoelastic interaction is the displacement gradient, not the strain as previously believed. The displacement gradient  $\frac{\partial u_\nu}{\partial X_\eta}$  can be decomposed into a symmetric part  $\frac{1}{2}(\frac{\partial u_\nu}{\partial X_\eta} + \frac{\partial u_\eta}{\partial X_\nu})$  which corresponds to a pure strain and an antisymmetric part  $\frac{1}{2}(\frac{\partial u_\nu}{\partial X_\eta} - \frac{\partial u_\eta}{\partial X_\nu})$  which corresponds to an infinitesimal rigid-body rotation. In birefringent materials, this rotation of volume elements varying within an acoustic wavelength will also contribute to the change in dielectric constant caused by an acoustic shear wave along a certain direction. In such a case the photoelastic coefficients no longer have the traditionally assumed symmetry upon interchange of the last two indices. Nelson and Lax derived the supplement term of photoelastic coefficients  $\Delta P_{ijkl}$ :

$$\Delta P_{ij(kl)} = \Delta P_{ji(kl)} = -\frac{1}{2} \left( \frac{1}{n_i^2} - \frac{1}{n_j^2} \right) (\delta_{ik} \delta_{jl} - \delta_{il} \delta_{jk}) \quad (71)$$

Nelson and Lax have verified their theories by carrying out measurements of photoelastic constants on strongly birefringent but non-piezoelectric materials like rutile (1970) and calcite (1972)<sup>[34]</sup>. The expression for  $P_{ijkl}$  in the most general case, then is

$$P_{ijkl}^* = P_{ijkl}^E - \frac{\sum_{n} r_{ij,n} \hat{q}_n \sum_{m} e_{m,ki} \hat{q}_m}{\sum_{m,n} \epsilon_{mn} \hat{q}_m \hat{q}_n} - \frac{1}{2} \left( \frac{1}{n_i^2} - \frac{1}{n_j^2} \right) (\delta_{ik} \delta_{jl} - \delta_{il} \delta_{jk}) \quad (72)$$

For lithium niobate, only the photoelastic coefficients  $P_{44}$  or  $P_{55}$  ( $P_{44} = P_{55}$ ) consist of both symmetric and anti-symmetric components.

Note that let  $P_{44} = \frac{1}{2} (P_{4,23} + P_{4,32})$  and  $P_{55} = \frac{1}{2} (P_{5,13} + P_{5,31})$ . Then, all formulas derived for a symmetric case remain valid. Corrections are made by adding the antisymmetric part:

$$P_{4,23} = P_{44} + \Delta P_{4,23} \quad (73a)$$

$$P_{4,32} = P_{44} + \Delta P_{4,32} = P_{44} - \Delta P_{4,23} \quad (73b)$$

#### Brillouin Scattering in RADP

RDP, ADP and RADP are all in the paraelectric phase at room temperature with a tetragonal point group symmetry of  $\bar{4}2m$  which belongs to the non-centrosymmetrical point group. They are piezoelectric at all temperatures. In

general, it is necessary to consider the secondary contribution to light scattering by the combined piezoelectric and electro-optic effect. The elastic ( $C_{ij}$ ), photoelastic ( $P_{mn}$ ), piezoelectric ( $e_{ik}$ ), and electro-optic ( $r_{hs}$ ) tensors are given as follows<sup>[24]</sup>:

$$(C_{ij}) = \begin{pmatrix} C_{11} & C_{12} & C_{13} & 0 & 0 & 0 \\ C_{12} & C_{11} & C_{13} & 0 & 0 & 0 \\ C_{13} & C_{13} & C_{33} & 0 & 0 & 0 \\ 0 & 0 & 0 & C_{44} & 0 & 0 \\ 0 & 0 & 0 & 0 & C_{44} & 0 \\ 0 & 0 & 0 & 0 & 0 & C_{66} \end{pmatrix} \quad (74)$$

There are six independent elastic coefficients.

$$(P_{mn}) = \begin{pmatrix} P_{11} & P_{12} & P_{13} & 0 & 0 & 0 \\ P_{12} & P_{11} & P_{13} & 0 & 0 & 0 \\ P_{31} & P_{31} & P_{33} & 0 & 0 & 0 \\ 0 & 0 & 0 & P_{44} & 0 & 0 \\ 0 & 0 & 0 & 0 & P_{44} & 0 \\ 0 & 0 & 0 & 0 & 0 & P_{66} \end{pmatrix} \quad (75)$$

There are seven independent photoelastic coefficients.

$$(e_{ik}) = \begin{pmatrix} 0 & 0 & 0 & e_{14} & 0 & 0 \\ 0 & 0 & 0 & 0 & e_{14} & 0 \\ 0 & 0 & 0 & 0 & 0 & e_{36} \end{pmatrix} \quad (76)$$

There are two independent piezoelectric coefficients.

$$(r_{hs}) = \begin{pmatrix} 0 & 0 & 0 \\ 0 & 0 & 0 \\ r_{41} & r_{41} & 0 \\ 0 & 0 & r_{63} \end{pmatrix} \quad (77)$$

There are two independent electro-optic coefficients.

For the  $\hat{q} = \frac{1}{\sqrt{2}}[110]$  and  $\hat{u} = \frac{1}{\sqrt{2}}(110)$  longitudinal

acoustic mode, the Brillouin scattering tensor is :

$$T^L = \frac{1}{2} \begin{pmatrix} \epsilon_0^2(P_{11}+P_{12}) & 2\epsilon_0^2P_{66} & 0 \\ 2\epsilon_0^2P_{66} & \epsilon_0^2(P_{11}+P_{12}) & 0 \\ 0 & 0 & 2\epsilon_0^2P_{31} \end{pmatrix} \quad (78)$$

with the effective elastic constant :

$$\rho v_L^2 = C_{66} + \frac{C_{11} + C_{12}}{2} \quad (79)$$

For the  $\hat{q} = \frac{1}{\sqrt{2}}[110]$  and  $\hat{u} = (001)$  transverse

acoustic mode the Brillouin scattering tensor is :

$$T_2^T = \frac{\epsilon_0 \epsilon_e}{\sqrt{2}} \begin{pmatrix} 0 & 0 & P_{44} \\ 0 & 0 & \pm P_{44} \\ P_{44} & \pm P_{44} & 0 \end{pmatrix} \quad (80)$$

with the effective elastic constant :

$$\rho v_T^2 = C_{44} \quad (81)$$

In a right angle scattering configuration, we can calculate the Rayleigh ratio for each of the  $[110]$  acoustic modes in RADP:

$$R^L(VV) = \frac{KT \omega_0^4}{32 \pi^2 c^4 \rho v_L^2} n_e^8 P_{31}^2 \quad (82)$$

$$R_2^T(VH) = \frac{1}{2} \frac{KT \omega_0^4}{32 \pi^2 c^4 \rho v_T^2} n_e^4 n_o^4 P_{44}^2 \frac{n_o}{n_e} \quad (83)$$

$$R^L(HH) = \frac{KT \omega_0^4}{32 \pi^2 c^4 \rho v_L^2} n_o^8 P_{66}^2 \quad (84)$$

$$R_2^T(HV) = \frac{1}{2} \frac{KT \omega_0^4}{32 \pi^2 c^4 \rho v_T^2} n_o^4 n_e^4 P_{44}^2 \frac{n_e}{n_o} \quad (85)$$

where the unit polarization vectors  $\hat{e}_o$  and  $\hat{e}_s$  for the incident and scattered light have the following values:

Incident vertical (V):  $\hat{e}_o = (001)$ ;

Incident horizontal (H):  $\hat{e}_o = (100)$ ;

Scattered vertical (V):  $\hat{e}_s = (001)$ ;

Scattered horizontal (H):  $\hat{e}_s = (010)$ .

The Rayleigh ratios of the first  $[110]$  transverse mode  $T_1$  are all zero for the above specifications.

The values of  $P_{31}$ ,  $P_{66}$  and  $P_{44}$  in the above formulas are their effective values. We need to use eq. (72) to determine the corrections due to the effects of the internal field and infinitesimal rigid-body rotation. For  $P_{31}$  and  $P_{66}$ , the second and third terms in right side of (72) are zero, therefore:

$$P_{31} = P_{31}^E \quad (86a)$$

$$P_{66} = P_{66}^E \quad (86b)$$

But for  $P_{44}$ , the two correction terms are both non-zero. We can decompose  $P_{44}$  into a symmetric part and a anti-symmetric part:

$$P_{4,23} = P_{44}^s + P_{4,23}^a \quad (87a)$$

$$P_{4,32} = P_{44}^s + P_{4,32}^a \quad (87b)$$

where superscript "s" stands for symmetric and superscript "a" stands for antisymmetric. According to eq. (71),

$$P_{4,23}^a = -P_{4,32}^a = \frac{1}{2} \left( \frac{1}{n_3^2} - \frac{1}{n_2^2} \right) = \frac{1}{2} \left( \frac{1}{n_e^2} - \frac{1}{n_o^2} \right) \quad (88)$$

This term is the correction corresponding to the pure rotation of the acoustic shear mode  $\left( \frac{\partial u_2}{\partial X_3} \right)$ . Because the piezoelectric and electro-optic coefficients of RADP are not available we have not calculated the second correction term in eq. (72).

## CHAPTER III

### EXPERIMENTAL APPARATUS AND PROCEDURE

#### Experimental Apparatus

The experimental apparatus used for Rayleigh-Brillouin scattering measurements is illustrated in Figure 6. The exciting source is a single mode argon-ion laser operating at 5145 Å. A multipass high contrast scanning Fabry-Perot interferometer is used for  $\geq 10^6$  resolving power with a photon-counting detecting system and associated data-handling electronics. The whole system ( laser, interferometer, and optics) is mounted on a air-supported vibration-isolated optical table. The detector consists of an ITT FW-130 photomultiplier tube with a S-20 photocathode which has a round 2.5 mm diameter effective area.

The output of the PMT is connected to the photon-counting electronics consisting of a Canberra model 814 Preamplifier-Amplifier-Discriminator (PAD) whose output is connected to both a ratemeter and a Burleigh DAS-10 system which is used to scan the Fabry-Perot and assure the long-term stability of the piezoelectric stacks of the Fabry-Perot. The amplifier output was also connected to a

BRILLOUIN SCATTERING SYSTEM WITH STABLE 3-PASS  
FABRY-PEROT INTERFEROMETER

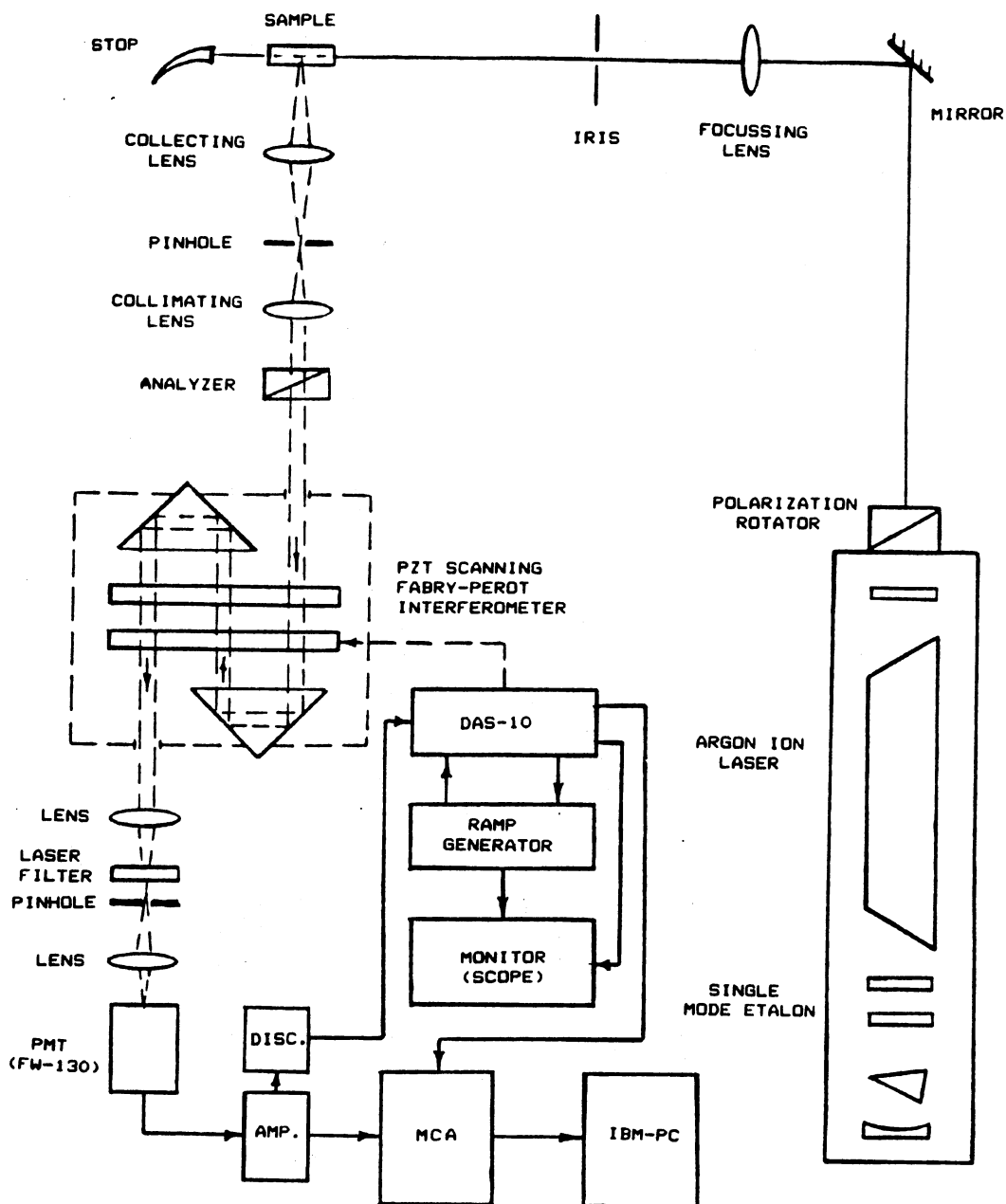


Figure 6. Schematic of Rayleigh-Brillouin Scattering Apparatus.

Canberra MCA for data acquisition. An IBM-XT was interfaced to the MCA for data storage and analysis.

#### Argon-ion Laser

A Spectra Physics model 2020 Argon-Ion laser was used and operated at a wavelength of 5145 Å. An etalon which acts as a bandpass filter is inserted in the cavity in order to isolate one single longitudinal mode with a linewidth of about 5 MHz. An adjustable iris diaphragm is located on the optic axis of the cavity to suppress all transverse modes except TEM<sub>00</sub>. In this single frequency, single mode operation, the maximum laser output power is 250-300mw, The stability of the laser output power is ± 0.5%. A single frequency output of the laser is critical for the delicate Brillouin scattering experiments in which the preliminary resolving power is 10<sup>2</sup> MHz.

#### Fabry-Perot Interferometer

A Burleigh model RC-110 Fabry-Perot interferometer was used in the experiments. It consists of a pair of air spaced fused silica plates in which the inner surfaces contain a high reflectivity coating at 450-550 nm with a flatness of  $\lambda/200$ . This PZT scanning resonant cavity interferometer is capable of extremely high resolution spectral analysis. The RC-110 allows 1-pass, 3-pass, or



5-pass operation. It is operated in triple pass with a throughput of  $\sim 43\%$  and a finesse of about 58 in our experiments.

#### Photomultiplier (PMT)

The very high gain, very low dark counting rate, and high sensitive in the visible spectrum range make the FW-130 PMT a suitable detector for photocounting in Rayleigh-Brillouin scattering experiments. The ITT FW-130 tube has the following important performance characteristics:

- A. Gain:  $5 \times 10^6$  (16 stages of dynodes)
- B. Spectral response: maximum at  $420 \pm 50$  nm, a quantum efficiency of 10.7 % at 5145 Å. (S-20 photocathode)
- C. Anode pulse rise time:  $\sim 10$  ns
- D. Dark counting rate: 1.0/s at  $T = -25^\circ\text{C}$ .

#### Multichannel Analyzer (MCA)

A Canberra series 35 plus multichannel analyzer was used for spectrum acquisition. It consists of a master controller and five sections: memory, display, signal processing, operator/MCA interface, and data input/output.

### Experimental Procedure

#### Sample Preparation

The samples used in these experiments were:

One fused quartz sample and two fluoride glass samples;  
One pure and one 0.2% Fe<sup>+3</sup> doped lithium niobate samples;  
Several RDP, ADP, and RADP samples.

All the samples were cut into rectangular parallelepipeds and the surfaces were polished to optical quality. The scattering geometries for the different samples are shown in Figure 7, Figure 8, and Figure 9.

The auxiliary parameters of refractive index and density were measured. The refractive index was measured by determining the angle of minimum deviation of a light ray through the sample. The top angle of each sample was cut in 90°, 60°, or 30° prism angles. The choice of the angle is determined by considering the total reflection angle and the proper sample shape. This prism angle was precisely measured using parallel rays being reflected from two faces of the prism (Fig. 10). A spectrometer S42561 and a linear polarized 5145 Å laser light source were used. The ray undergoes refraction by this prism shaped sample. From the measured minimum deviation angle the refractive indices of the sample were calculated (Fig. 11).

The densities of the samples were determined by an Archimedean technique where the distilled water or spectroscopic grade cyclohexane was used as a working fluid. The results obtained are shown in Table I.

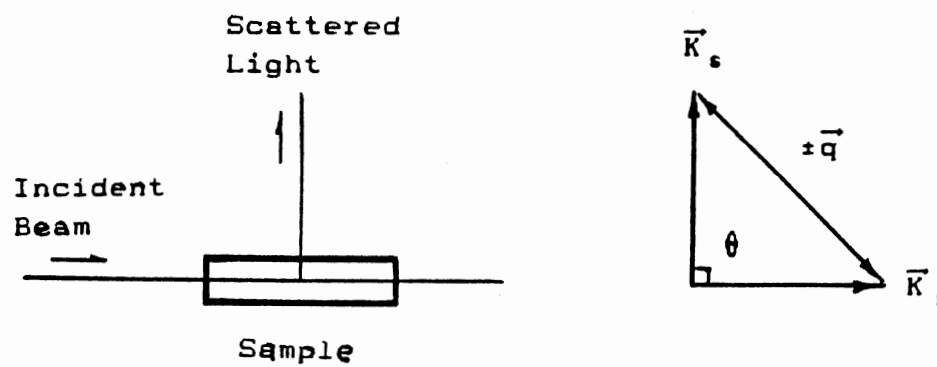
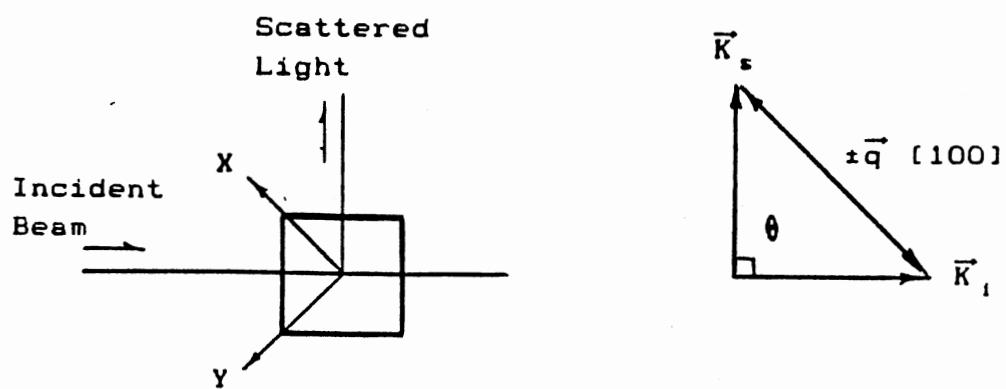
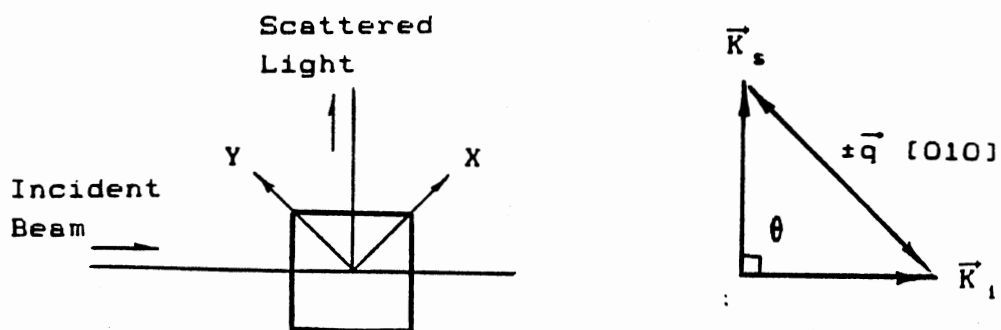


Figure 7. Top View of the Scattering Geometry and the Wavevector Relations for Glass Sample.



(a) [100] Phonon Scattering



(b) [010] Phonon Scattering

Figure 8. Top View of the Scattering Geometry and the Wavevector Relations for the Lithium Niobate Sample. The C-axis is Perpendicular to XY-Plane.

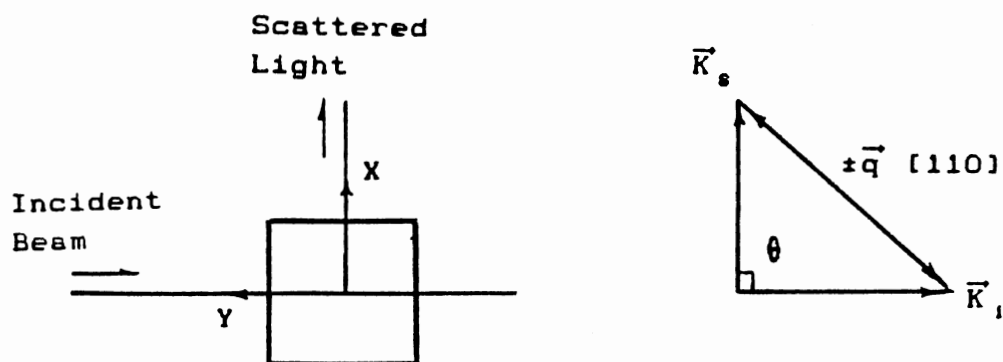


Figure 9. Top View of the Scattering Geometry and the Wavevector Relations for the RADP Sample. [110] Phonon Scattering, the C-axis is Perpendicular to XY-Plane.

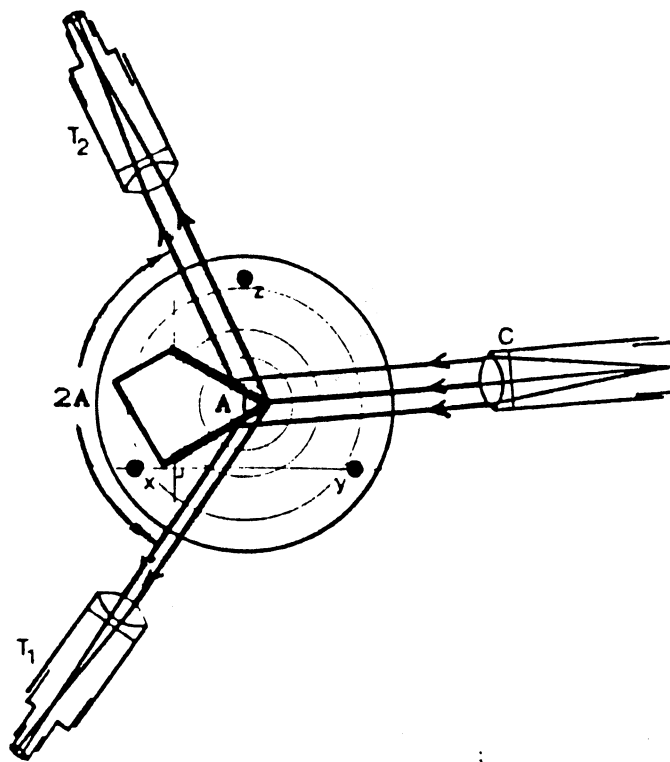
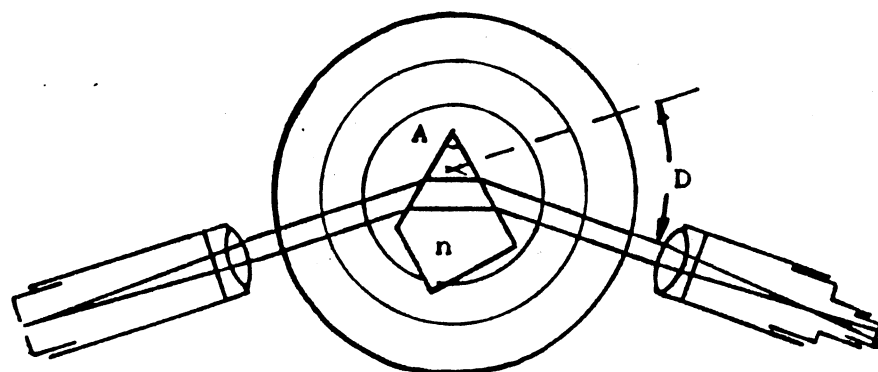
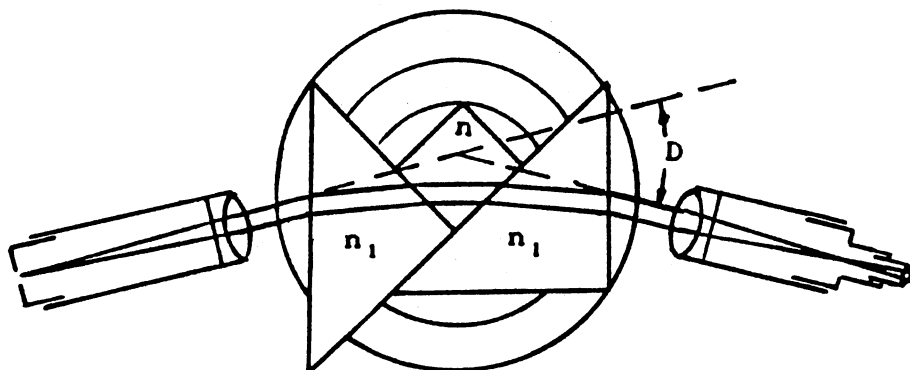


Figure 10. Arrangement for Measuring the Angle Between the Two Faces of the Sample.



(a) Arrangement 1: 
$$n = \frac{\text{SIN } \frac{1}{2}(A+D)}{\text{SIN } \frac{1}{2}A}$$



(b) Arrangement 2: 
$$n = \text{SIN}\left(\frac{D}{2}\right) + [n_1^2 - \text{SIN}^2\left(\frac{D}{2}\right)]^{1/2}$$

Figure 11. Arrangements for Measuring the Refractive Index of the Sample by Determining the Minimum Deviation Angle D.

TABLE I  
THE DENSITIES AND THE REFRACTIVE INDICES  
OF THE SAMPLES

(A). Glasses:				
Samples	$\rho$ (g/cm <sup>3</sup> )	$n$		
Fused Quartz	2.205	1.462		
ZBL AN	4.353	1.508		
BZL	6.464	1.538		
(B). Crystals:				
Samples	$\rho$ (g/cm <sup>3</sup> )	$n_o$	$n_e$	$\bar{n}$
LiNbO <sub>3</sub>	4.647	2.335	2.240	2.288
LiNbO <sub>3</sub> +0.2%Fe <sup>3+</sup>	4.659	2.330	2.241	2.286
ADP	1.796	1.529	1.482	1.506
RADP(48%)	2.217	1.522	1.482	1.502
RADP(42%)	2.288	1.521	1.482	1.502
RADP(28%)	2.451	1.517	1.482	1.500
RDP	2.869	1.512	1.481	1.497

**Notes:**

- (1).  $\rho$  stands for the density of the material.
- (2).  $n$  is the refractive index of the isotropic material;  $n_o$  and  $n_e$  are the refractive indices of birefringent material for ordinary and extraordinary polarized light, respectively.
- (3).  $\bar{n} = \sqrt{\frac{1}{2}(n_o^2 + n_e^2)}$
- (4). All refractive indices are measured at the wavelength of  $\lambda = 5145 \text{ \AA}$ .



### Setting the Free Spectral Range (FSR):

The spectral display obtained with a FP is repetitive. Consecutive Rayleigh peaks obtained correspond to consecutive integer values of the order of interference. The range of frequencies within this interval is termed the "Free Spectral Range (FSR)". The constructive interference condition of the FP is

$$\frac{1}{\lambda} = \text{integer} \cdot \frac{1}{2d} \quad (86)$$

where  $\lambda$  is the wavelength of the incident light and  $d$  is the plate separation of the FP. Thus the FSR is determined by the plate separation:

$$\text{FSR} = \frac{1}{2d} \quad (87)$$

### Choosing the Fore Pinhole and Laser Filter

A spatial filter allowed the precise definition of the scattering volume in each data run. The selection of the fore pinhole which acts as a spatial filter in front of the FP is very important. It is desirable to have the pinhole small enough to block unwanted spurious scattered light but large enough to collect as much light as possible. Increasing the pinhole diameter too much will also degrade the system finesse due to a decrease in pinhole finesse. we usually choose a pinhole size of 50  $\mu\text{m}$  or 75  $\mu\text{m}$  in the experiments except in the case of detecting the weak TA peak of the fluoride glasses, where

the intensity was a problem and a 200 $\mu$ m pinhole was used resulting in a smaller finesse.

A 1 nm bandwidth laser filter centered on the 5145 Å wavelength, was placed before the pinhole to block out most background and high-frequency Raman-scattered light.

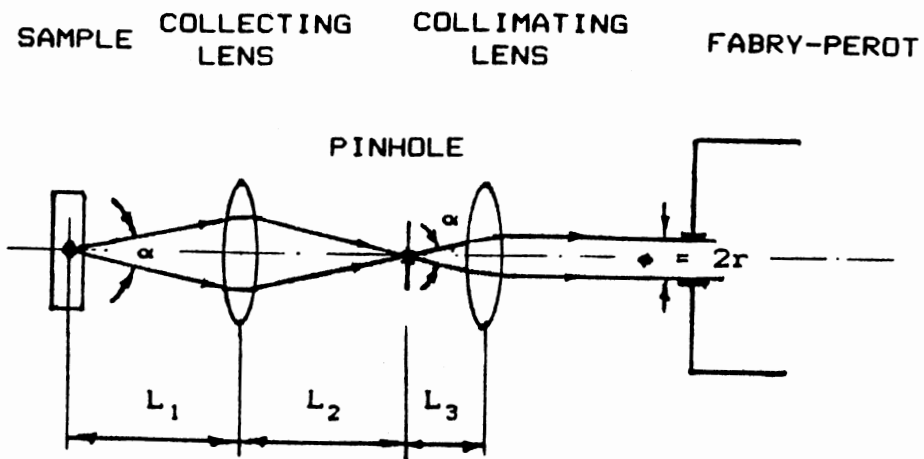
#### Determination of Measured Quantities

The solid angle in which the scattered light was collected is determined by the aperture of the FP and the collection optics, which includes a 5.5cm focal length Olympus camera lens used to collect the scattered light, a pinhole used as a spatial filter, and a 5.0cm Olympus camera lens used to collimate the collected light. (Fig. 12).

The primary quantities that are measured in this study are the Brillouin shifts and the peak intensities. The determination of these quantities from the Brillouin spectrum is shown in Fig. 13. The figure displays a two order Brillouin spectrum of the fused quartz sample. The calculations are executed by a computer data analysis program written in Turbo Basic<sup>[38]</sup>.

#### Weak TA Signal Detection

In the Brillouin spectrum of the heavy metal fluoride glasses, the TA peaks are very weak. The intensities of the TA peaks were two orders of magnitude smaller than



$$L_1 = L_2 = 11 \text{ cm}$$

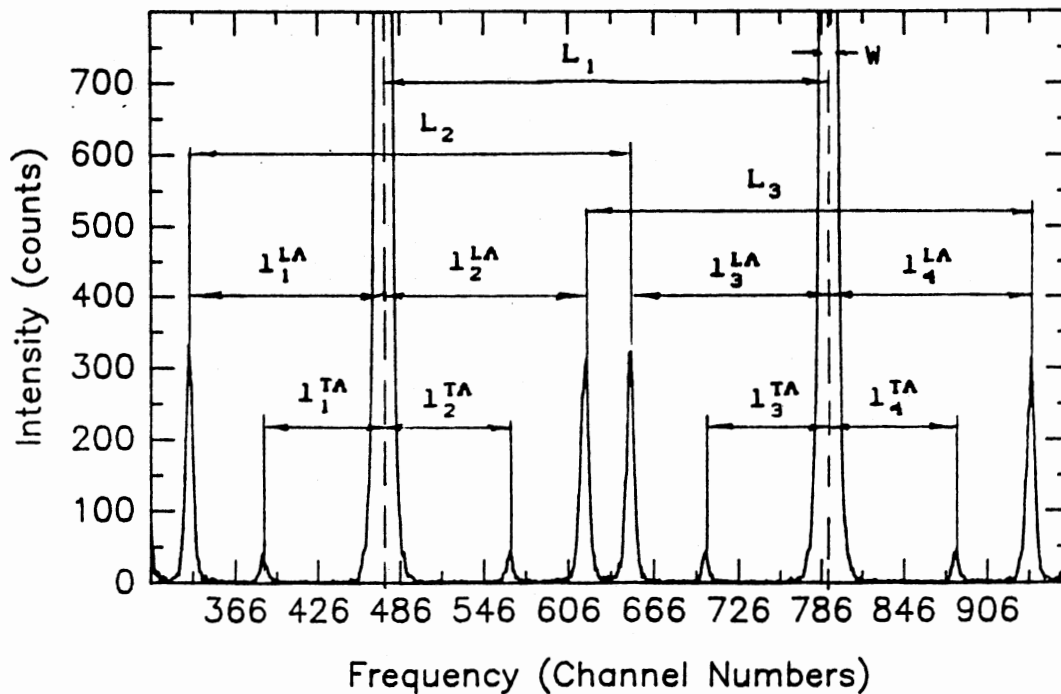
$$L_3 = 5.0 \text{ cm}$$

$$\diamond = 2r = 1.1 \text{ cm}$$

The Collecting Solid Angle:  $\Omega = \frac{\pi r^2}{L_3^2} = 0.038 \text{ rad.}$

The Cross Section Angle:  $\alpha = 2 \text{ Arctan} \left( \frac{r}{L_3} \right) = 12.55 \text{ deg.}$

Figure 12. The Collecting Angle.



FP Separation:  $d$

$$FSR = \frac{1}{2d}$$

$$FSR \text{ in Channel Number: } L = \frac{1}{3}(L_1 + L_2 + L_3)$$

Full Width at Half Maximum:  $W$

$$\text{Finesse: } \frac{L}{W}$$

$$\text{LA Shift in Channel Number: } 1^{LA} = \frac{1}{4}(1_1^{LA} + 1_2^{LA} + 1_3^{LA} + 1_4^{LA})$$

$$\text{TA Shift in Channel Number: } 1^{TA} = \frac{1}{4}(1_1^{TA} + 1_2^{TA} + 1_3^{TA} + 1_4^{TA})$$

Brillouin Shifts ( $\text{cm}^{-1}$ ):

$$(K_0)^{LA} = \frac{1^{LA}}{L} \times FSR$$

$$(K_0)^{TA} = \frac{1^{TA}}{L} \times FSR$$

Brillouin Intensities (counts under peak contour):

$I^{LA}$ : The Area of LA Peak

$I^{TA}$ : The Area of TA Peak

Figure 13. Procedure for Determining the Primary Quantities in the Brillouin Spectrum.

that of the LA peaks in our spectrum. This is why the transverse components of the heavy metal fluoride glasses were reported as "difficult to measure"<sup>[8]</sup> or "unable to record"<sup>[9]</sup> in previous papers.

Resolution and detectivity which specifies a signal-to-noise ratio are two important figures of merit in the spectrum detection. Here we discuss the signal to noise ratio for weak acoustic component detection and give several suggestions to improve our technique in Brillouin scattering experiments.

The background counts in the Brillouin spectrum come from four sources: the dark counts of the PMT which are dominated by the cathode dark current<sup>[35]</sup>, the thermal radiation by the environment through the view field of the PMT, the fluorescence radiation of the sample in the bandwidth of the laser filter and the preamplifier noise. Because the thermal radiation is mostly distributed in the infrared region which is beyond the spectral response of S-20 cathode, it can be ignored. Because of the very high gain ( $10^6$ ) of the PMT, the noise from the preamplifier can also be ignored. Let  $N_d$  denote the number of dark counts per channel from the PMT and  $N_f$  denote the number of fluorescence counts per channel from the sample, while  $n_d$  and  $n_f$  denote these same quantities in the units of counts/second. For our experimental conditions,  $n_d = 1.0$  count/s and  $n_f = 36.7$  counts/s for the ZBL fluoride glass sample. Because of the random nature of the electron

emission events (i.e., photoemission, thermal emission, or field induced emission)<sup>[35]</sup>, the background counts per observation interval obey the Poisson distribution<sup>[36]</sup>:

$$p(N) = \frac{(\bar{N})^N}{N!} e^{(-\bar{N})} \quad (88)$$

where  $p(N)$  is the probability of  $N$  counts being detected in a given observation time in which the average number of counts detected is  $\bar{N}$ . The mean square fluctuation of the background counts:

$$\langle \Delta N \rangle^2 = \langle (N - \bar{N}) \rangle^2 = \bar{N} \quad (89)$$

which indicate that the root-mean-square (rms) fluctuation (noise) in counts per channel is equal to the square root of the mean counts per channel. If the Brillouin components are too weak, they will be obscured by the background fluctuations. This happened in the case of the weak transverse components of the fluoride glasses. For independent fluctuation sources, we have:

$$\langle \Delta N \rangle^2 = \langle \Delta N_d \rangle^2 + \langle \Delta N_f \rangle^2 \quad (90)$$

If we want to have a significant signal to noise ratio, say signal/noise = 5, the signal counts per channel need to be 5 times that of the rms fluctuation of the background counts.

There are several ways to increase the signal to noise ratio for weak Brillouin component detection:

A. Increase the laser power.

Both signal counts (Brillouin component) and the mean value of background counts  $N_f$  will increase approximately proportional to laser power, while the dark

counts  $N_d$  will not change. Because the background noise equals the square root of the mean value, if we increase the laser power  $m$  times, the signal to noise ratio will at least increase by a factor of  $(m)^{\frac{1}{2}}$ . In our experiments we used a laser power of 250 mw which is the maximum output power available for 5145 Å single mode operation of the 2020 Argon-ion laser.

B. Increase scattering volume by increasing the size of fore pinhole.

In our case the higher laser power was not available because the limitation of the instrument. We increased the fore pinhole size from 50  $\mu\text{m}$  to 200  $\mu\text{m}$  in diameter. It greatly increased both the signal and background counts and hence increased the ratio of signal to background fluctuation. The cost of increasing the pinhole size is that the finesse of the spectrum was reduced from 58 to 38.

C. Increase accumulation time.

Since each Brillouin peak results from a single frequency, the signal of the same Brillouin component are correlated in time. When we increase the accumulation time  $m$  times the average counts of Brillouin peak will increase  $m$  times. However, the background fluctuations are white in this frequency region and are not correlated in time. When we increase the accumulation time  $m$  times the rms fluctuation only increases  $(m)^{\frac{1}{2}}$ . We use 10,000 sweeps of the 0.5s scan period, a total accumulation time

of 5,000 seconds, to obtain both a good signal to noise ratio and good statistics for the TA peaks of the fluoride glass.



## CHAPTER IV

### RESULTS AND ANALYSIS

#### Fluoride Glasses

The Brillouin spectra of the fused quartz and two  $\text{Eu}^{3+}$ -doped fluoride glasses ZBLAN and BZL are shown in Fig.14, 15, 16, respectively. These spectra were obtained using right angle scattering configurations at the specified incident-scattered polarizations. The compositions of the two heavy metal fluoride glass samples are given in table II. The basic measured quantities in Brillouin scattering are shown in table III and the final results are given in the table IV.

We calculated the sound velocities by using eq. (10) and then determined the elastic constants by the following equations:

$$C_{11} = \rho (v_L)^2 \quad (91a)$$

$$\text{and } C_{44} = \rho (v_T)^2 \quad (91b)$$

The Poisson's ratio is also determined by use of the equation:

$$\sigma = \frac{C_{11} - 2C_{44}}{2(C_{11C} - C_{44})} = \frac{(\Delta\omega_L)^2 - 2(\Delta\omega_T)^2}{2[(\Delta\omega_L)^2 - (\Delta\omega_T)^2]} \quad (92)$$

where  $\Delta\omega_L$  and  $\Delta\omega_T$  are the longitudinal and transverse

Brillouin shifts, respectively.

The sound velocities of both the longitudinal and transverse modes in the fluoride glasses are significant smaller than that in fused quartz. This indicates that these fluoride glasses have a much softer lattice than fused quartz. The smaller shear elastic constant  $C_{44}$  and higher Poisson's ratio of the fluoride glasses also indicate the more flexible structure. This is due to their atomic bonding: the covalent bonds of the tetrahedra  $\text{SiO}_4$  in the fused quartz are more rigid and do not bend easily, while the mostly close packed<sup>[37]</sup> ionic bonds in fluoride glasses are less rigid.

The photoelastic constant  $P_{12}$  was determined by the intensity ratio of the longitudinal Brillouin components of the fluoride glass to that of fused quartz, while  $P_{44}$  was determined by the intensity ratio of the transverse Brillouin components of the fluoride glass to that of fused quartz (Appendix B). This is done by recording the Brillouin spectra of fused quartz and fluoride glass under the exact same conditions. The given value  $P_{12}$  of fused quartz was measured in our Lab. by G. H. Gangwere<sup>[38]</sup>.

Because the fluoride glass samples have some absorption in the 5145 Å region, the intensity of scattered light is related to the distance light travels through the sample as follows:

$$I(L) = I_0 e^{-\alpha L} \quad (93)$$

where  $\alpha$  is the absorption coefficient and  $L=Y_0+x$  is the total distance that the incident and scattered light travel through the sample (Fig. 17). We repeat the experiments by changing the scattering volume position  $x$  within the sample. We then use a linear regression routine to extrapolate the intensities to  $L=0^+$  position and determine the absorption coefficient  $\alpha$  and the intensity ratio  $\eta_{LA}$  (Fig. 18). The absorption coefficients of two fluoride glasses so determined are  $\alpha_{ZBL AN} = 0.11 \text{ cm}^{-1}$  and  $\alpha_{BZL} = 0.15 \text{ cm}^{-1}$ . For a path  $L = 0.3 \text{ cm}$  these absorption coefficients will cause a correction of about 3.2% and 4.4%, respectively.

We successfully recorded the intensities and shifts of the TA peaks for both fluoride glass samples and determined the values of photoelastic constants  $P_{44}$ . We found that the  $P_{44}$  of the fluoride glass is less than one sixth of the  $P_{44}$  of fused quartz. It is interesting to note that the values of  $P_{12}$  obtained by us for two fluoride samples were in good agreement with the values reported in Fig. 4 of Schroeder's paper<sup>[8]</sup>. However the  $P_{44}$  values obtained were only about 1/6 of the  $P_{44}$  values given by Schroeder in the same graph. Schroeder declared that the transverse  $P_{44}$  coefficients were rather small and difficult to measure while he gave the  $P_{44}$  of fluoride glass a value similar to that of fused quartz.

The big difference in the  $P_{44}$  values between the fluoride glass and fused quartz is attributed to their

different bonding and different type of structure. According to the theory given by Mueller<sup>[39]</sup> and Carleton<sup>[40]</sup> the photoelastic coefficients  $P_{11}$  and  $P_{12}$  associated with compressional strains have a direct density dependence while the  $P_{44}$  associated with shear strain has no direct density dependence. This is why the  $P_{12}$  in fluoride glasses are about two-thirds of the  $P_{12}$  value of fused quartz, whereas  $P_{44}$  are less than one-sixth of their counterparts in the fused quartz. The  $P_{44}$  represents the change of the local dielectric constant by the shear distortion. In a more flexible and highly coordinated structure of the fluoride glass, the shear strain causes less local field change. Hence the  $P_{44}$  of the fluoride glasses is much smaller than the  $P_{44}$  in fused quartz.

The scattering loss is calculated from a combination of Brillouin data and the Landau-Placzek ratio. The Brillouin scattering loss  $\alpha_b$  is given by<sup>[41]</sup>:

$$\alpha_b = \frac{8\pi^3}{3} \frac{KT}{\lambda_0^4} \frac{(n^4 P_{12})^2}{C_{11}} \quad (94)$$

and the Rayleigh scattering loss becomes

$$\alpha_s = \alpha_b (R_{L.P.} + 1) \quad (95)$$

where  $R_{L.P.}$  is the Landau-Placzek ratio. To express the Rayleigh attenuation in db/km, one simply multiplies  $\alpha_s$  by  $-4.34 \times 10^5$ .

It can be seen that the ZBLAN sample has a Rayleigh scattering loss of 20.7 db/km which is comparable to the

Rayleigh scattering loss of fused quartz (9.94 db/km) and to that of the fluoride glass (15.2 db/km) reported by Grishin<sup>[9]</sup>. According to the scattering theory (Eq.31), the scattering loss is proportional to  $\lambda^{-4}$ . These fluoride glasses exhibit a minimum in optical absorption in the 2-4  $\mu\text{m}$  spectral region<sup>[42]</sup>. The extrapolation of the Rayleigh scattering loss of ZBLAN at  $\lambda = 3.0 \mu$  gives  $\sim 1.8 \times 10^{-2}$  db/km. This optical loss is much smaller than that of fused quartz at  $\lambda = 1.55 \mu$ , where the optical losses are minimal, which gives  $\sim 1.2 \times 10^{-1}$  db/km. Another fluoride glass sample BZL exhibits much higher Rayleigh scattering. We saw many bright spots distributed inside the scattering volume. Therefore, it may be attributed to the devitrification during the sample growth. If devitrification has started, the crystal grains will act as additional scattering centers, and if they become very dense, then multiple elastic scattering will set in.

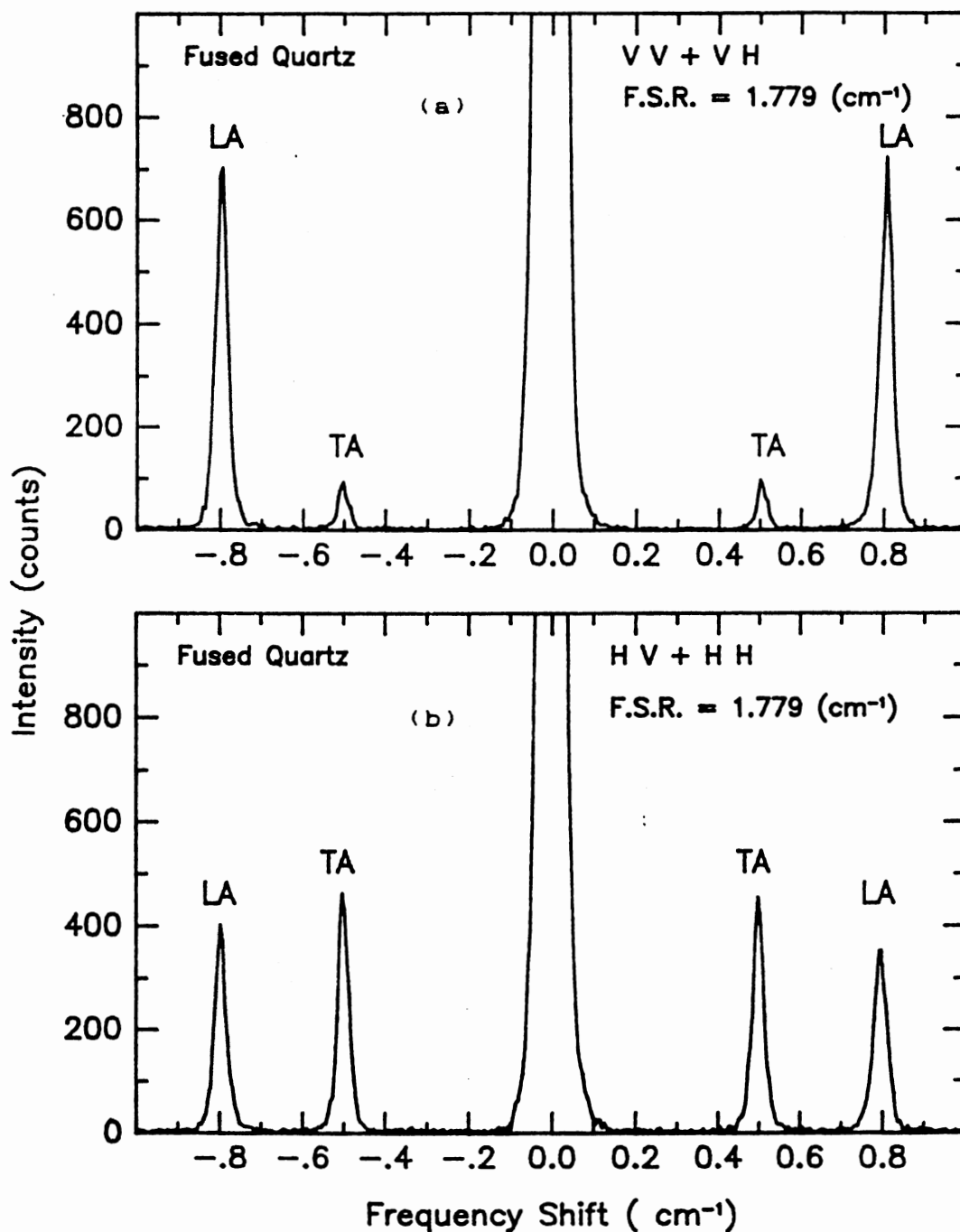


Figure 14. Brillouin Spectra of Fused Quartz.

(a) Incident Light is Vertical Polarized and Scattered Light is Unpolarized.

(b) Incident Light is Horizontal Polarized and Scattered Light is Unpolarized.

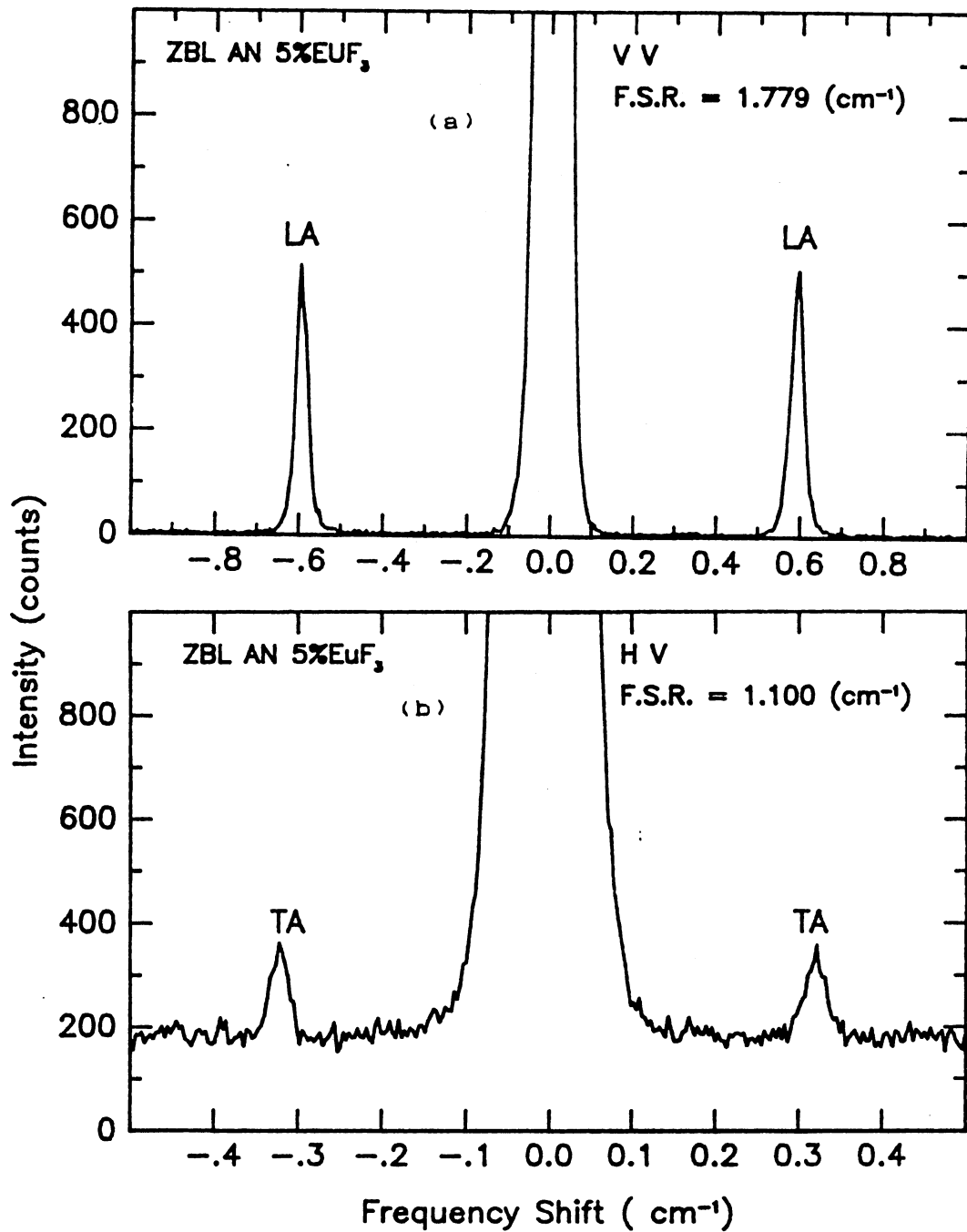


Figure 15. Brillouin Spectra of ZBL AN Fluoride Glass.  
 (a) Both Incident Light and Scattered Light are Vertical Polarized  
 (b) Incident Light is Horizontal Polarized and Scattered Light is Vertical polarized.

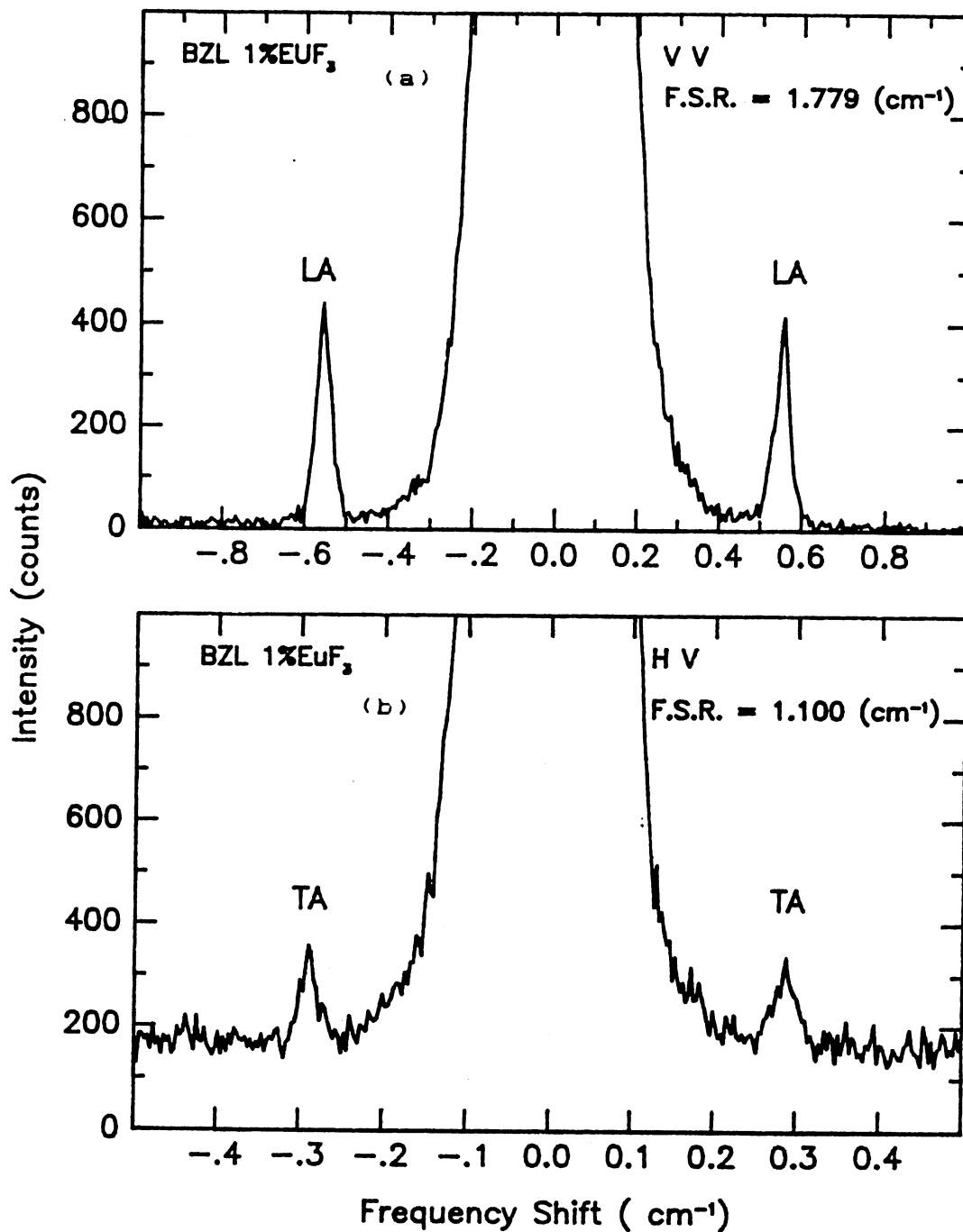


Figure 16. Brillouin Spectra of BZL Fluoride Glass.  
 (a) Both Incident Light and Scattered Light are Vertical Polarized  
 (b) Incident Light is Horizontal Polarized and Scattered Light is Vertical polarized.



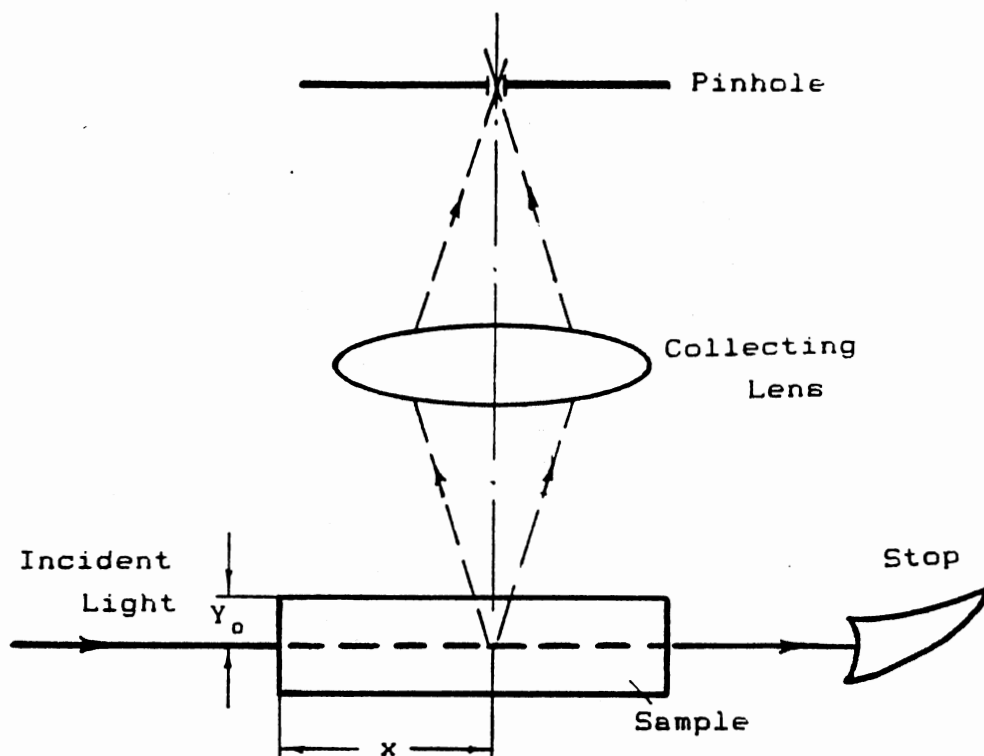


Figure 17. The Configurations of Measuring Brillouin Intensities with Changing Light Path  $x$  Inside A Sample.

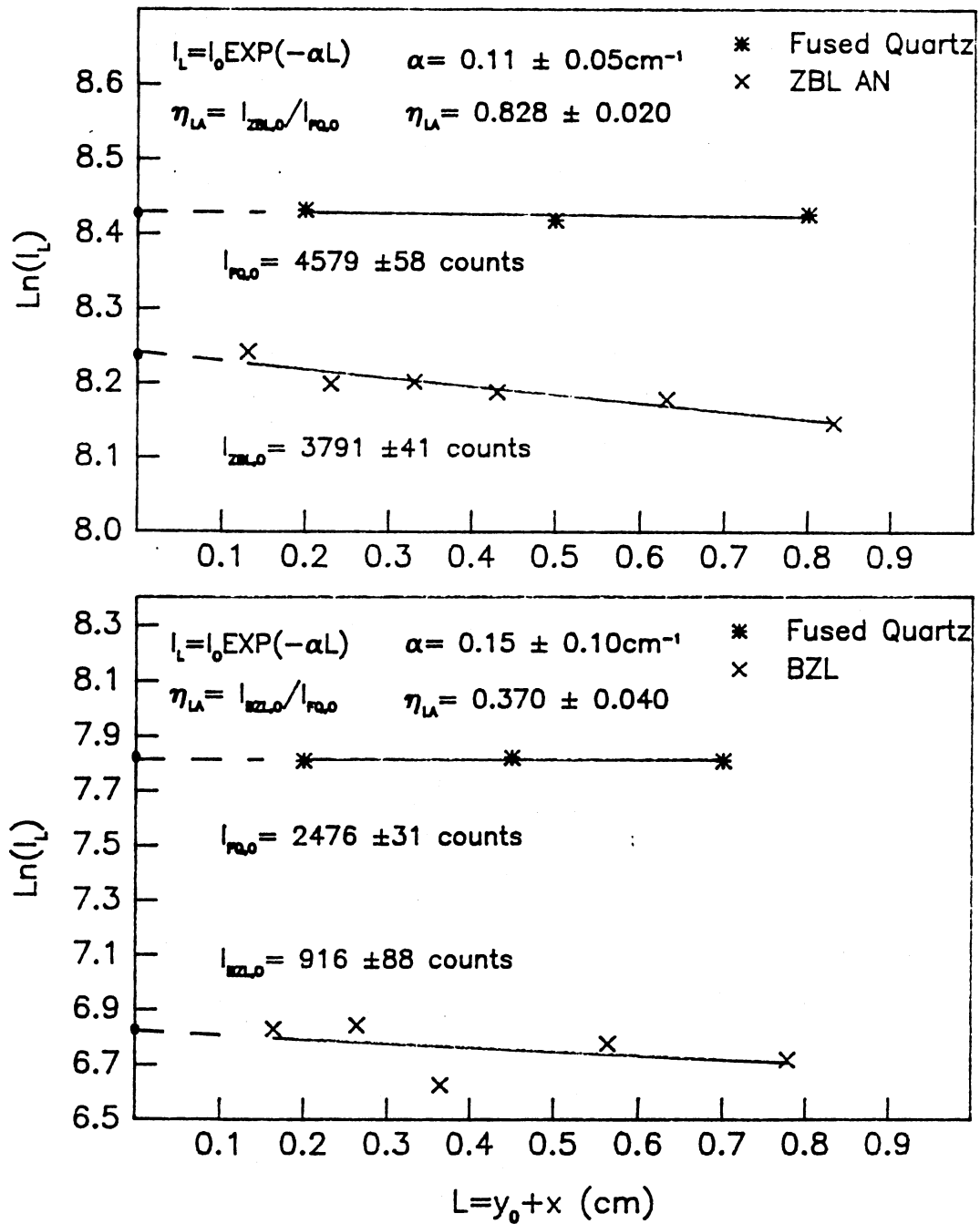


Figure 18. Longitudinal Brillouin Intensity  $I_L$  Versus the Light Traveled Distance  $L$  Inside the Sample.  
 (a) Fused Quartz and Fluoride Glass ZBL AN.  
 (b) Fused Quartz and Fluoride Glass BZL.

TABLE II

THE CONSTITUENTS OF TWO FLUORIDE GLASS SAMPLES  
(Mol. Percentage)

Glass	ZrF <sub>4</sub>	BaF <sub>2</sub>	LaF <sub>3</sub>	AlF <sub>3</sub>	NaF	EuF <sub>3</sub>
ZBL AN	53.01	13.68	5.51	3.61	19.19	5.00
Glass	BaF <sub>3</sub>	ZnF <sub>2</sub>	LuF <sub>3</sub>	ThF <sub>4</sub>	EuF <sub>3</sub>	
BZL	19.0	27.0	26.0	27.0	1.0	

TABLE III

BASIC MEASURED QUANTITIES IN BRILLOUIN SCATTERING

Samples	$\Delta\omega_L$ (cm <sup>-1</sup> )	$\Delta\omega_T$ (cm <sup>-1</sup> )	$I_T^0/I_L^0$	$I_L/I_L^0$	$I_T/I_T^0$	$R_{LP}$
ZBL AN	0.596	0.322		0.828	0.0378	51.7
BZL	0.556	0.289		0.370	0.0364	1.06X10 <sup>4</sup>
Fused Quartz	0.799	0.502	0.101			21.6

## Notes:

- (i).  $\Delta\omega$ : Brillouin Shift (for the wavelength  $\lambda=5145\text{\AA}$ ).
- (ii). I: Brillouin Intensity.
- (iii).  $R_{LP}$ : Landau-Placzek ratio.
- (iv). Superscript 'o' denotes the measured values from fused quartz, subscript 'L' denotes LA mode and subscript 'T' denotes TA mode.

TABLE IV

SOUND VELOCITIES, ELASTIC CONSTANTS AND POISSON'S RATIOS  
( $\sigma$ ) OF TWO FLUORIDE GLASSES AND FUSED QUARTZ

Samples	$v_L$	$v_T$	$C_{11}$	$C_{44}$	$\sigma$
	$10^5 \text{cm/s}$	$10^5 \text{cm/s}$	$10^{10} \text{dyn/cm}^2$	$10^{10} \text{dyn/cm}^2$	
ZBL AN	4.31	2.33	$80.9 \pm 0.4$	$23.6 \pm 0.3$	0.294
BZL	3.94	2.05	$100.4 \pm 0.5$	$27.2 \pm 0.3$	0.315
Fused Quartz	5.96	3.75	$78.3 \pm 0.4$	$30.9 \pm 0.3$	0.174

TABLE V

PHOTOELASTIC CONSTANTS AND SCATTERING LOSS OF  
TWO FLUORIDE GLASSES AND FUSED QUARTZ

Samples	$P_{12}$	$P_{44}$	Scattering loss** (db/km)
	ZBL AN	$0.236 \pm 0.008$	$(1.23 \pm 0.09) \times 10^{-2}$
BZL	$0.167 \pm 0.010$	$(1.22 \pm 0.16) \times 10^{-2}$	$19.5 \pm 2.4 \times 10^2$
Fused Quartz	$0.279^*$	$0.0787 \pm 0.0020$	$9.94 \pm 0.50$

\*  $P_{12}$  of fused quartz was measured by G.H.Gangwere<sup>[38]</sup>  
in our Lab..

\*\* For wavelength  $\lambda = 5145 \text{\AA}$ .

## Lithium Niobate

The [100] phonon spectra of the pure and 0.2% Fe<sup>3+</sup> doped Lithium Niobate are shown in Fig. 19 and 20, respectively. These spectra were obtained from the right angle scattering configuration at the specified incident-scattered polarizations. The elastic constant  $C_{11}$  is then determined by:

$$C_{11} = \rho (v_L)^2 \quad (96)$$

We determine  $C_{66} = \rho (v_T)^2$  by using the TA[010] phonon scattering and solve  $C_{12}$  by:

$$C_{12} = C_{11} - 2C_{66} \quad (97)$$

As indicated in Chapter II, elastic constants so determined satisfy  $C_{11} = C_{11}^E$  and  $C_{66} = C_{66}^E$ .

The photoelastic constants  $P_{31}$  and  $P_{41}$  were determined by measuring the intensity ratio of the longitudinal Brillouin components from the [100] phonon scattering of Lithium Niobate to that of fused quartz (Appendix B). The photoelastic constants so determined satisfy  $P_{31} = P_{31}^E$  and  $P_{41} = P_{41}^E$ . The basic measured quantities, the sound velocities and elastic constants, and the photoelastic constants  $P_{31}$ ,  $P_{41}$  are shown in Table VI to Table VIII.

We notice that the elastic constants of the Fe-doped sample have similar values to that of the pure sample. We believe that the Fe<sup>3+</sup> atom goes either into Nb or Li site because these two sites are both axially symmetric about

the c-axis<sup>[43]</sup>. It is easy to understand that the doped sample has similar elastic constants to the pure sample because the 0.2% Fe<sup>3+</sup> impurity should not change the lattice structure of Lithium Niobate much. However the Brillouin intensities from 0.2% Fe doped sample are only 43% of that from the pure sample (TABLE VI). This is mainly caused by the much stronger absorption at  $\lambda=5145\text{\AA}$  in the Fe-doped sample than in the pure sample. We roughly measured the absorption at  $\lambda=5145\text{\AA}$  for both samples. The absorption coefficients are  $\sim 5.2\text{cm}^{-1}$  for Fe-doped sample and  $\sim 0.15\text{cm}^{-1}$  for pure sample. This absorption has been attributed to intervalence transfer from the Fe<sup>2+</sup> ions to next-nearest-neighbour Nb<sup>5+</sup> ions<sup>[44]</sup>.

Lithium Niobate is one of the important elasto-optic materials used for acousto-optic devices. The crystal is usually oriented in a 35° Y-cut plate for maximizing the figure-of-merit in device applications<sup>[45][5]</sup>. The optical beam propagating in  $\vec{k}$  direction is polarized at an angle of 35° relative to the y-axis with a longitudinal acoustic wave propagating along the x-axis (Fig. 21). Under this configuration we calculate the effective  $n$ ,  $p$ ,  $v$  as follows:

$$n = \sqrt{(n_o^2 \cos^2 35^\circ + n_e^2 \sin^2 35^\circ)} \quad (98)$$

$$v = v^{L[100]} \quad (99)$$

$$p = \frac{1}{n^4} [\hat{e}_s T^{L[100]} \hat{e}_o]$$

$$= \frac{1}{n^4} [\text{COS}^2 35^\circ n_o^4 P_{12} + 2 \text{SIN} 35^\circ \text{COS} 35^\circ n_o^2 n_s^2 P_{41} + \text{SIN}^2 35^\circ n_e^4 P_{31}]$$

(100)

where we use  $P_{12} = 0.072$  from R.W.Dixon<sup>[5]</sup>. In comparing the usefulness of acoustic-optical materials for device applications, four figures of merit have been developed<sup>[46]</sup>:

$$M_1 = \frac{n^7 p^2}{\rho v} \quad (101a)$$

$$M_2 = \frac{n^6 p^2}{\rho v^3} \quad (101b)$$

$$M_3 = \frac{n^7 p^2}{\rho v^2} \quad (101c)$$

$$M_4 = \frac{n^8 p^2 v}{\rho} \quad (101d)$$

The figures of merit can be normalized relative to fused quartz, which has the following absolute values for the four figures of merit as obtained from our experiment data:

$$M_1 = 8.46 \times 10^{-7} [\text{cm}^2 \text{ s g}^{-1}]$$

$$M_2 = 1.63 \times 10^{-18} [\text{s}^3 \text{ g}^{-1}]$$

$$M_3 = 1.42 \times 10^{-12} [\text{cm s}^2 \text{ g}^{-1}]$$

$$M_4 = 4.39 \times 10^5 [\text{cm}^4 \text{ s}^{-1} \text{ g}^{-1}]$$

The acousto-optic figures of merit for the pure Lithium Niobate sample so determined are listed in Table IX.

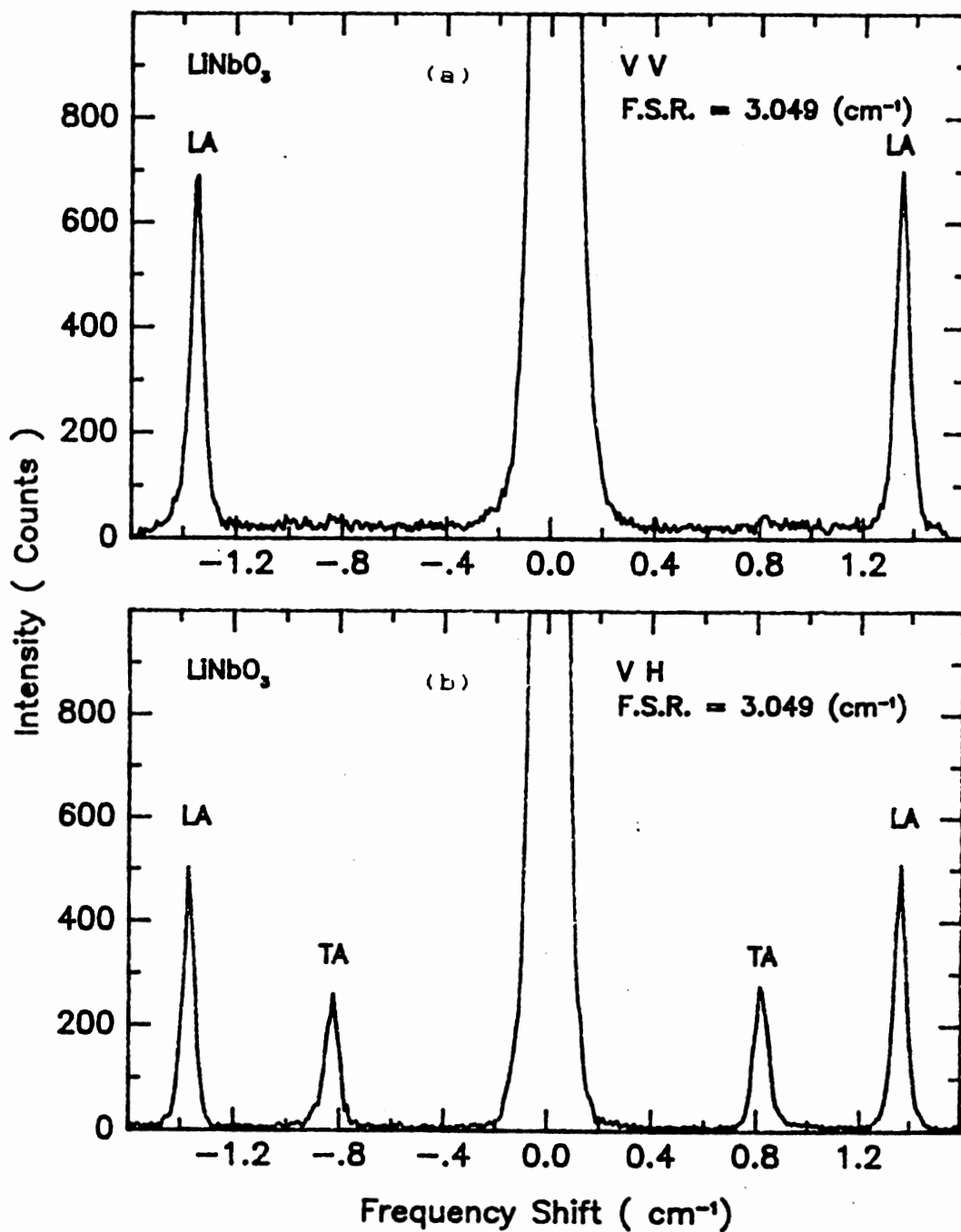


Figure 19. The [100] Phonon Spectra of the Pure  $\text{LiNbO}_3$ .  
 (a) Both Incident and Scattered Light are Polarized  $\parallel$  to C-axis.  
 (b) Incident Light is Polarized  $\parallel$  to C and Scattered Light is Polarized  $\perp$  to C.



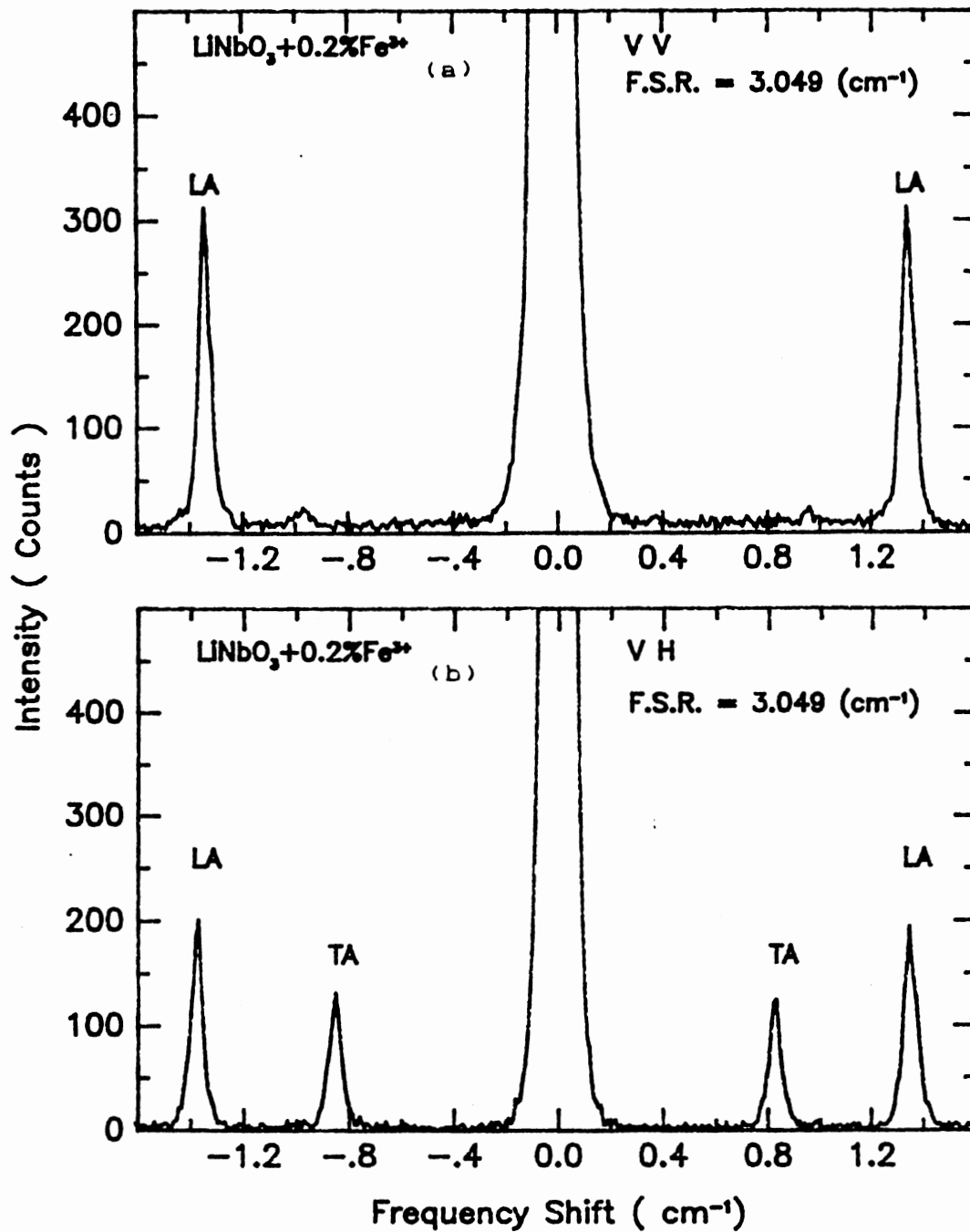


Figure 20. The [100] Phonon Spectra of 0.2% Fe-doped  $\text{LiNbO}_3$ .

(a) Both Incident and Scattered Light are Polarized  $\parallel$  to C-axis.

(b) Incident Light is Polarized  $\parallel$  to C and Scattered Light is Polarized  $\perp$  to C.

TABLE VI

THE BASIC MEASURED QUANTITIES IN BRILLOUIN SCATTERING  
(Lithium Niobate)

(A). [100] Phonon Scattering:

Samples	$\Delta\omega_{vv}^L$ ( $\text{cm}^{-1}$ )	$\Delta\omega_{vh}^L$ ( $\text{cm}^{-1}$ )	$I_{vv}^L/I_{vv}^o$	$I_{vh}^L/I_{vv}^o$
LiNbO <sub>3</sub>	1.35	1.37	1.25	0.809
LiNbO <sub>3</sub> +0.2%Fe <sup>3+</sup>	1.35	1.37	0.575	0.332

(B). [010] Phonon Scattering:

Samples	$\Delta\omega_{vv}^L$ ( $\text{cm}^{-1}$ )	$\Delta\omega_{vh}^T$ ( $\text{cm}^{-1}$ )
LiNbO <sub>3</sub>	1.38	0.819
LiNbO <sub>3</sub> +0.2%Fe <sup>3+</sup>	1.38	0.820

Notes:

- (i).  $\Delta\omega$ : Brillouin Shift (for the wavelength  $\lambda=5145\text{\AA}$ )
- (ii). I: Brillouin Intensity.
- (iii). Superscript 'o' denotes the measured values from fused quartz, superscript 'L' denotes LA mode.
- (iv). Subscripts 'vv', 'vh' denote the incident-scattering polarizations of the light.

TABLE VII

SOUND VELOCITIES AND ELASTIC CONSTANTS  
(Lithium Niobate)

Samples	$v^{L[100]}$	$C_{11}^E$	$v^{T[010]}$	$C_{66}^E$	$C_{12}^E$
	$10^5(\frac{\text{cm}}{\text{s}})$	$10^{10}(\frac{\text{dyn}}{\text{cm}^2})$	$10^5(\frac{\text{cm}}{\text{s}})$	$10^{10}(\frac{\text{dyn}}{\text{cm}^2})$	$10^{10}(\frac{\text{dyn}}{\text{cm}^2})$
LiNbO <sub>3</sub>	6.573	201±1	3.91	71.0±0.4	58.9±0.8
LiNbO <sub>3</sub> + 0.2% Fe	6.570	201±1	3.91	71.3±0.4	58.3±0.8

TABLE VIII

PHOTOELASTIC CONSTANTS  $P_{31}$  AND  $P_{41}$   
(Lithium Niobate)

Samples	$P_{31}^E$	$P_{41}^E$
LiNbO <sub>3</sub>	0.157±0.008	0.168±0.008

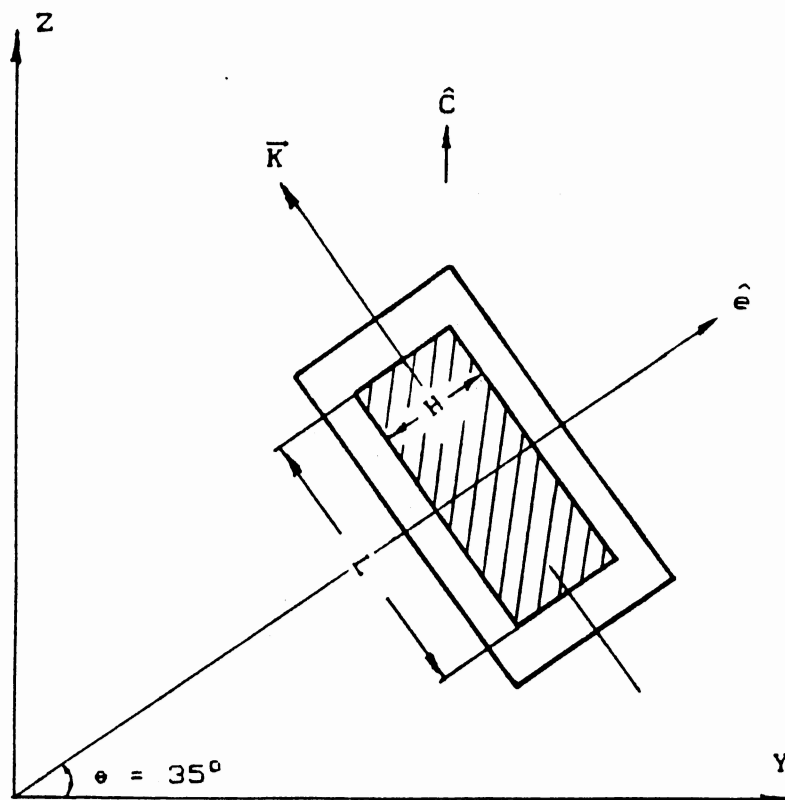


Figure 21. The  $35^\circ$  Y-cut Configuration of Lithium Niobate for Device Applications.

TABLE IX

THE ACOUSTO-OPTIC FIGURES OF MERIT  
(Lithium Niobate and Fused Quartz)

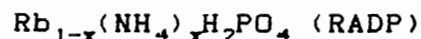
(A) The Effective Values of $n$ , $v$ , and $P$ in a $35^\circ$ Y-cut Plate.					
Samples	Acoustic Polarization Mode Direction		$n$	$v$ $10^5(\text{cm/s})$	$P$
LiNbO <sub>3</sub>	L[100]	35°Y-Z	2.304	6.573	0.250
Fused Quartz	L[100]		1.462	5.96	0.279

(B) The Acousto-Optic Figures of Merit.				
Samples	$M_1$ $10^{-7}$ (cm <sup>2</sup> sg <sup>-1</sup> )	$M_2$ $10^{-18}$ (s <sup>3</sup> g <sup>-1</sup> )	$M_3$ $10^{-12}$ (cms <sup>2</sup> g <sup>-1</sup> )	$M_4$ $10^5$ (cm <sup>4</sup> s <sup>-1</sup> g <sup>-1</sup> )
LiNbO <sub>3</sub>	70.5	7.08	10.7	70.2
Fused Quartz	8.46	1.63	1.42	4.39

(C) The Normalized Figures of Merit Relative to Fused Quartz.				
Samples	$\bar{M}_1$	$\bar{M}_2$	$\bar{M}_3$	$\bar{M}_4$
LiNbO <sub>3</sub>	8.33	4.34	7.54	16.0



The room temperature [110] phonon spectra of RADP were obtained from the right angle scattering configuration at specified incident-scattered polarizations for  $x=0.0, 0.28, 0.42, 0.48$  and  $1.0$ , respectively. The [110] Brillouin spectra with increasing ammonium concentration are illustrated in Figure 22. It shows that the frequency shifts are increasing and the intensities are decreasing with increasing ammonium component  $x$ .

The effective elastic constant of the LA[110] mode is then determined by

$$\frac{1}{2}(C_{11}+C_{12})+C_{66} = \rho(v^L)^2 \quad (102)$$

and the elastic constant  $C_{44}$  is determined by

$$C_{44} = \rho(v^T)^2 \quad (103)$$

The results of the sound velocities and elastic constants are listed in Table XI. According to the values we obtained, the effective elastic constant along [110] direction  $[\frac{1}{2}(C_{11}+C_{12})+C_{66}]$  increase linearly with the ammonium concentration  $x$ , while the shear elastic constant  $C_{44}$  decrease with the ammonium concentration  $x$ . These relations are shown in Figure 23. The answer to these elastic constant changes lies on the bonding relations of RADP. The RADP system belongs to the KDP family. ADP and RDP are isomorphic at room temperature. The structure of

RADP at room temperature is shown in Fig. 24 (a) and (b). The projection of the  $PO_4$  tetrahedra is on the xy plane. The P atoms lie at the center of each tetrahedron at the heights marked. The O atoms are positioned at the four vertices of each tetrahedron. The  $Rb^+$  or  $(NH_4)^+$  lie at height  $c/2$  above P atoms. The dotted lines show the hydrogen bonds and the broken lines show the outline of the unit cell. In RDP, the  $Rb^+$  is bonded to eight neighboring O atoms which belong to the six  $PO_4$  tetrahedrons, including those that lie at  $\pm c/2$  above and below  $Rb^+$ . When  $Rb^+$  is replaced by  $(NH_4)^+$ , the  $(NH_4)^+$  has only four protons which form the hydrogen bonds between N and four nearest O atoms which belong to four neighboring  $PO_4$  tetrahedrons, not including those that lie at  $\pm c/2$  above and below  $(NH_4)^+$  (Fig. 24 (c)). Therefore, after  $(NH_4)^+$  replaced  $Rb^+$  the bonds among cells are weaker along c-axis direction and stronger along the directions perpendicular to c-axis. The larger values of elastic constant along [110] indicates the stronger bonding along xy direction and the smaller value of  $C_{44}$  ( $C_{44} = C_{55}$ ) indicates that the z-planes are easier to shear along y-direction or x-direction.

The photoelastic constants  $P_{31}$  were determined by measuring the intensity ratio of the LA[110] of RADP sample to that of fused quartz, while  $P_{44}$  and  $P_{66}$  were determined by measuring the intensity ratio of the TA[110] to LA[110] for specialized incident-scattered

polarizations (Appendix B). The results are listed in Table XII(A). The photoelastic constant  $P_{31}$  decreases with the increasing ammonium concentration  $x$  as shown in Figure 25.

As we discussed in Chapter II, the photoelastic constant  $P_{44}$  consists of both symmetric and antisymmetric components and must be expressed as two separate coefficients:  $P_{4,23}$  and  $P_{4,32}$ . The antisymmetric component caused by the effects of small rigid-body rotation is:

$$\Delta P_{4,23} = \frac{1}{2} \left( \frac{1}{n_3^2} - \frac{1}{n_2^2} \right) = \frac{1}{2} \left( \frac{1}{n_e^2} - \frac{1}{n_o^2} \right) \quad (103)$$

and

$$P_{4,23} = P_{44} + \Delta P_{4,23} \quad (104a)$$

$$P_{4,32} = P_{44} - \Delta P_{4,23} \quad (104a)$$

The  $P_{4,23}$  and  $P_{4,32}$  values of different RADP samples are listed in Table XII(B) which shows that the corrections are around 23% to 33% of the  $P_{44}$  value. Therefore, the effects of small rigid-body rotation are significant and cannot be ignored in determining the  $P_{4,23}$  and  $P_{4,32}$  values of RADP.



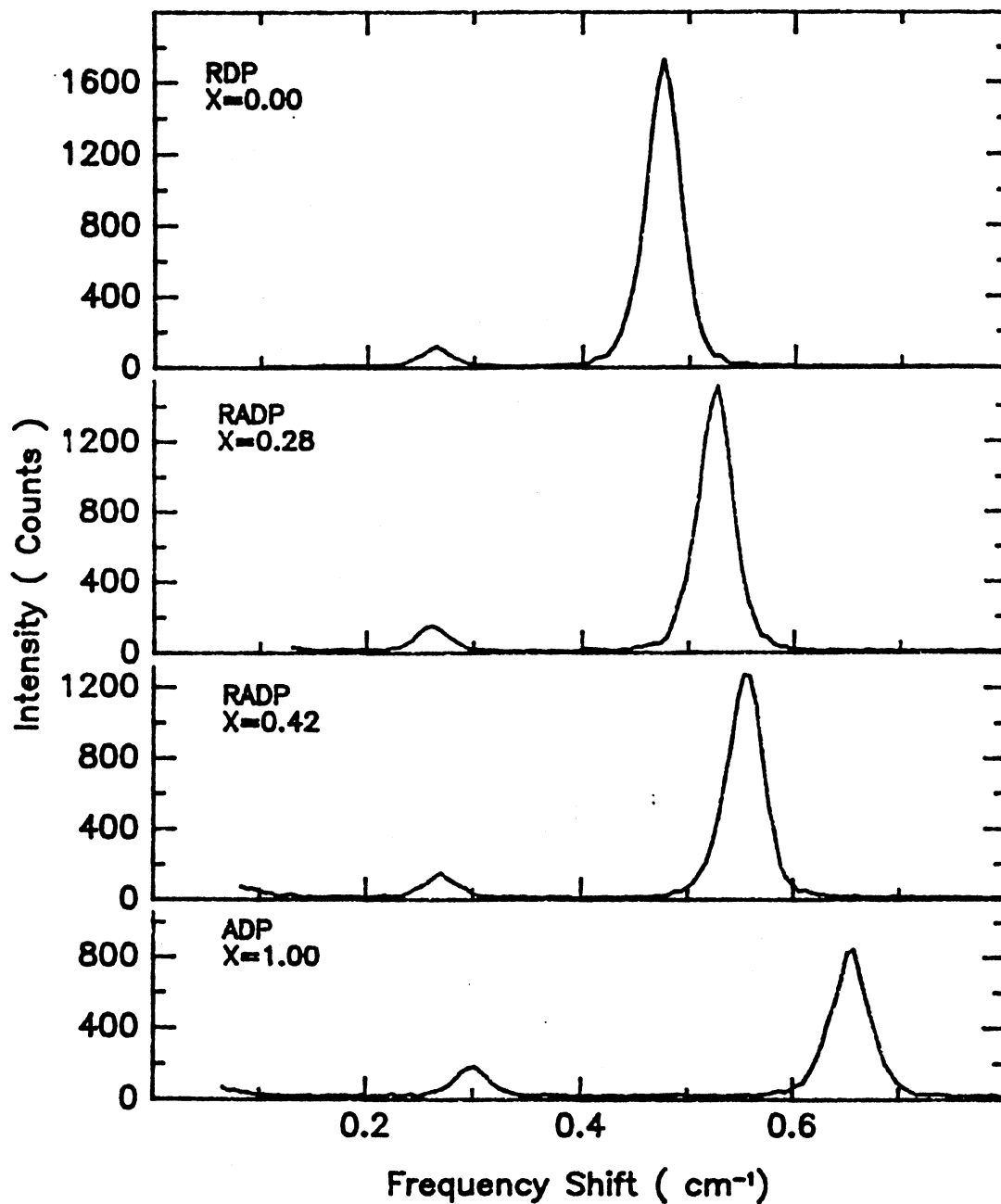


Figure 22. The [110] Phonon Spectra of  $\text{Rb}_{1-x}(\text{NH}_4)_x\text{H}_2\text{PO}_4$  ( $\lambda=5145\text{\AA}$ ). The Incident Light is Polarized  $\parallel$  to C-axis and the Scattered Light is Unpolarized.

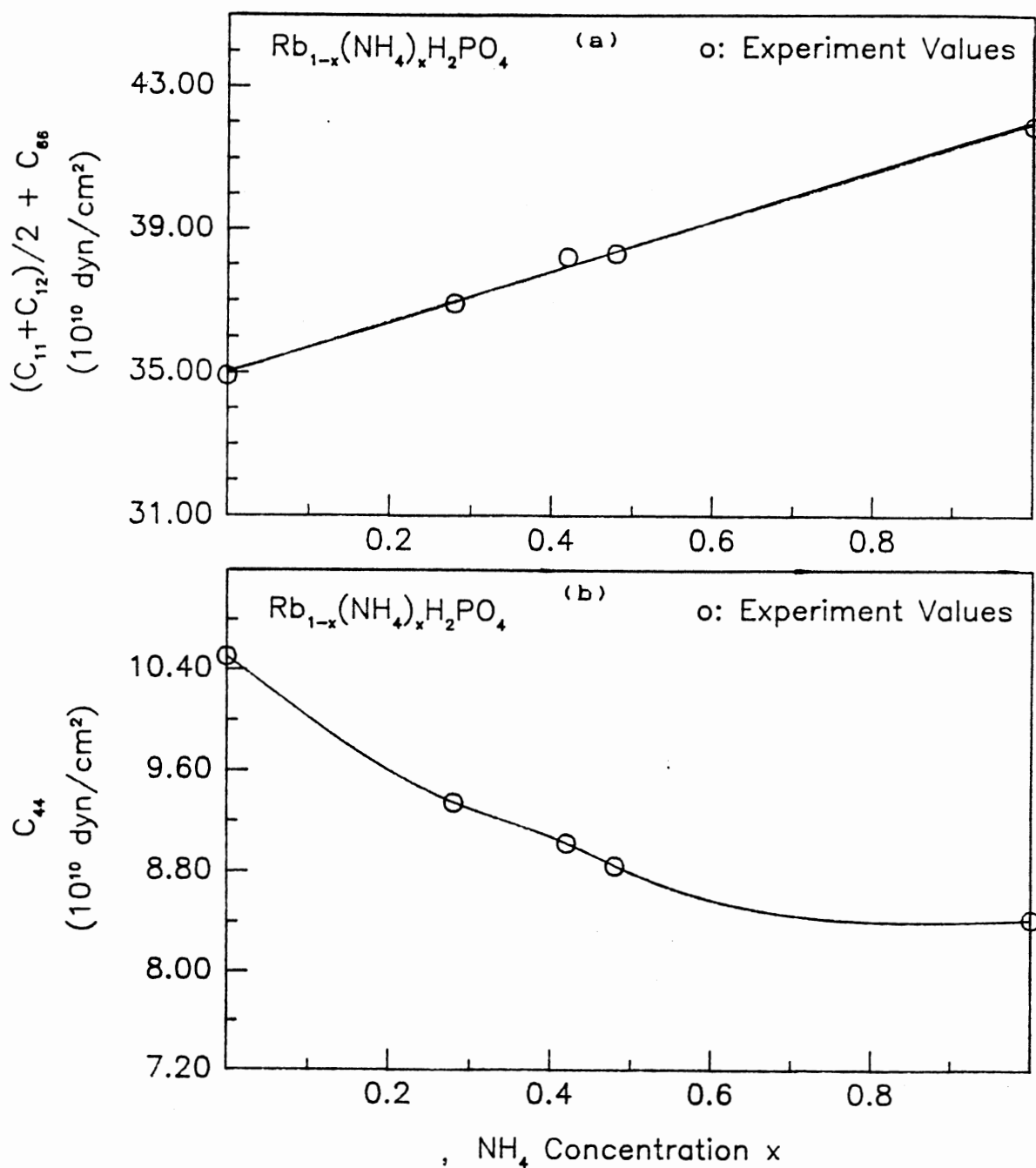


Figure 23. The Elastic Constants Versus Ammonium Concentration  $x$ .

(a)  $\frac{1}{2}(C_{11}+C_{12})+C_{66}$  Versus  $x$

(b)  $C_{44}$  Versus  $x$ .

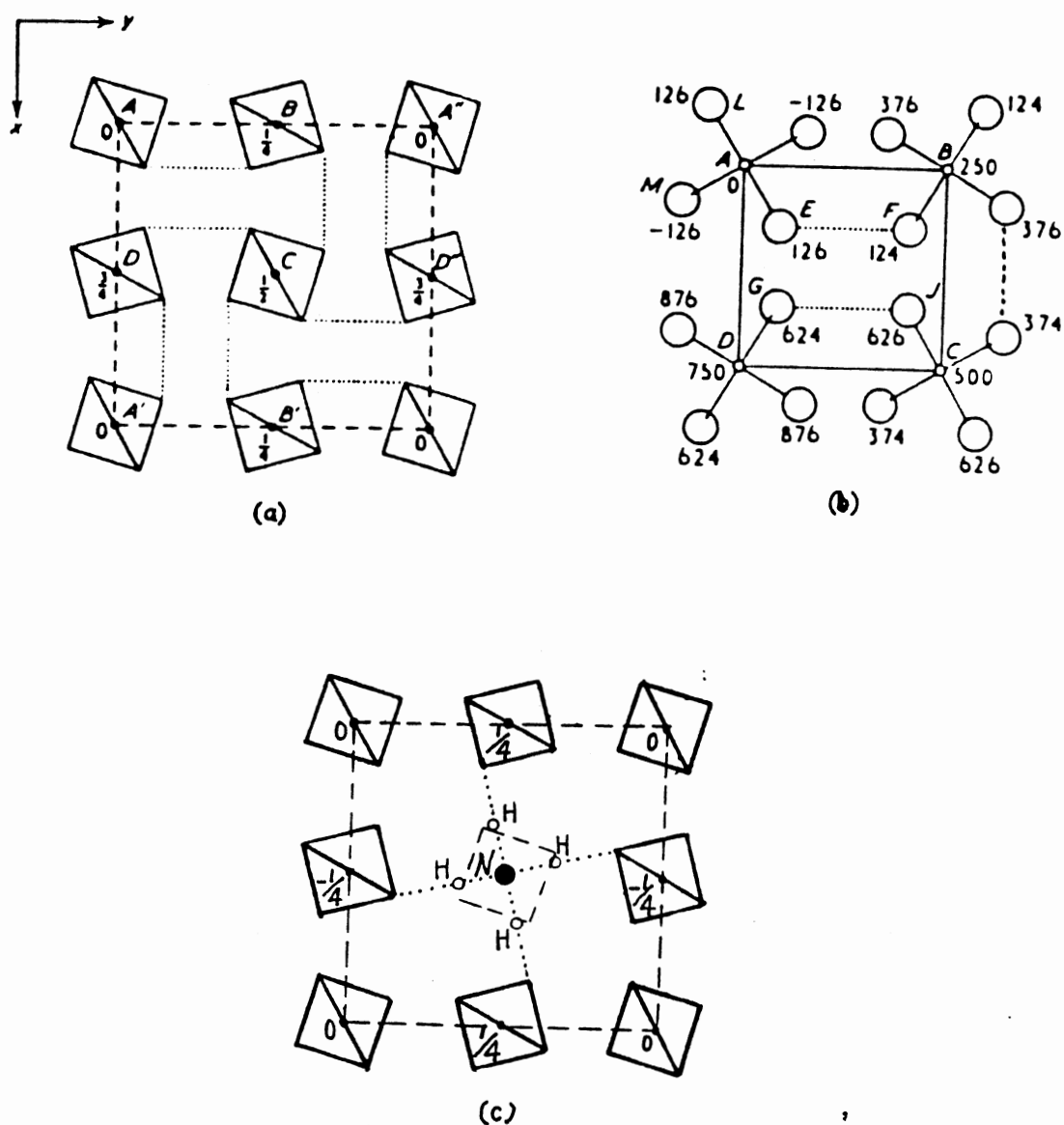


Figure 24. The Structure and Bonding of RADP.  
 (a) Projection on [001] of PO<sub>4</sub> tetrahedra of RADP at Room Temperature. (b) Part of Projection Drawn on A Large Scale.  
 (c) N-H-O bonds among (NH<sub>4</sub>)<sup>+</sup> and four tetrahedra.

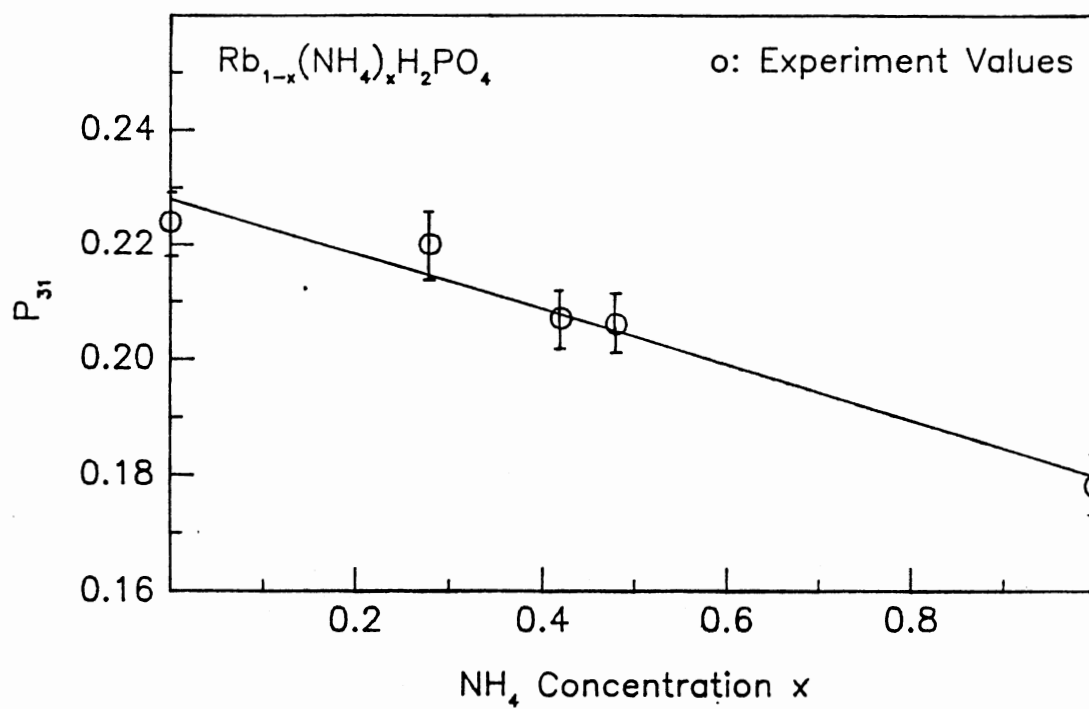


Figure 25. The Photoelastic Constant  $P_{31}$  Versus Ammonium Concentration  $x$

TABLE X

THE BASIC MEASURED QUANTITIES IN BRILLOUIN SCATTERING  
 (  $\text{Rb}_{1-x}(\text{NH}_4)_x\text{H}_2\text{PO}_4$  [110] Phonon )

## (A) Brillouin Shifts.

Samples	$\Delta\omega_{\text{VV}}^{\text{L}}$ $\text{cm}^{-1}$	$\Delta\omega_{\text{hh}}^{\text{L}}$ $\text{cm}^{-1}$	$\Delta\omega_{\text{vh}}^{\text{T}}$ $\text{cm}^{-1}$	$\Delta\omega_{\text{hv}}^{\text{T}}$ $\text{cm}^{-1}$
ADP	0.656	0.673	0.299	0.298
RADP(X=0.48)	0.567	0.577	0.276	0.274
RADP(X=0.42)	0.556	0.570	0.273	0.274
RADP(X=0.28)	0.527	0.543	0.268	0.269
RDP	0.474	0.484	0.263	0.262

## (B) Brillouin Intensity Ratio.

Samples	$I_{\text{VV}}^{\text{L}}/I_{\text{VV}}^{\text{O}}$	$I_{\text{vh}}^{\text{T}}/I_{\text{VV}}^{\text{L}}$	$I_{\text{hh}}^{\text{L}}/I_{\text{hv}}^{\text{T}}$
ADP	0.819	0.151	1.30
RADP(X=0.48)	1.19	0.0964	1.51
RADP(X=0.42)	1.21	0.0944	1.76
RADP(X=0.28)	1.42	0.0850	1.74
RDP	1.55	0.0561	1.95

TABLE XI

SOUND VELOCITIES AND ELASTIC CONSTANTS  
(  $\text{Rb}_{1-x}(\text{NH}_4)_x\text{H}_2\text{PO}_4$  [110] Phonon )

Samples	$v^L$ $10^5(\frac{\text{cm}}{\text{s}})$	$v^T$ $10^5(\frac{\text{cm}}{\text{s}})$	$\frac{1}{2}(C_{11}+C_{12})+C_{66}$ $10^{10}(\frac{\text{dyn}}{\text{cm}^2})$	$C_{44}$ $10^{10}(\frac{\text{dyn}}{\text{cm}^2})$
ADP	4.83	2.17	41.9±0.4	8.42±0.08
RADP(X=0.48)	4.17	2.00	38.3±0.4	8.84±0.09
RADP(X=0.42)	4.09	1.99	38.2±0.4	9.02±0.09
RADP(X=0.28)	3.88	1.95	36.9±0.4	9.34±0.09
RDP	3.49	1.91	34.9±0.4	10.5±0.10

TABLE XII

PHOTOELASTIC CONSTANTS OF  $\text{Rb}_{1-x}(\text{NH}_4)_x\text{H}_2\text{PO}_4$

(A)  $P_{31}$ ,  $P_{44}$  and  $P_{66}$ .

Samples	$P_{31}(10^{-1})$	$P_{44}(10^{-2})$	$P_{66}(10^{-2})$
ADP	1.78±0.06	4.19±0.15	7.19±0.25
RADP(X=0.48)	2.06±0.07	4.18±0.15	7.27±0.25
RADP(X=0.42)	2.07±0.07	4.19±0.15	7.79±0.28
RADP(X=0.28)	2.20±0.07	4.40±0.15	7.93±0.28
RDP	2.24±0.07	4.00±0.15	7.01±0.24

(B)  $P_{4,23}$  and  $P_{4,32}$ .

Samples	$\Delta P(10^{-2})$	$P_{4,23}(10^{-2})$	$P_{4,32}(10^{-2})$
ADP	1.38±0.03	2.81±0.18	5.57±0.18
RADP(X=0.48)	1.18±0.02	3.00±0.17	5.36±0.17
RADP(X=0.42)	1.15±0.02	3.04±0.17	5.35±0.17
RADP(X=0.28)	1.04±0.02	3.36±0.17	5.44±0.17
RDP	0.925±0.02	3.07±0.17	4.92±0.17

## CHAPTER V

### SUMMARY AND CONCLUSION

In this thesis, Brillouin scattering investigations of the elastic and photoelastic constants of two fluoride glasses and two ferroelectric materials, Lithium niobate and RADP, have been reported.

We have successfully measured the Brillouin intensities and shifts of two heavy metal fluoride glasses, ZBL AN and BZL. Values of the  $C_{11}$  and  $C_{44}$  elastic constants have been obtained and yield Poisson's Ratios which indicate that these glasses have higher coordination numbers and softer lattices than fused quartz. Rayleigh scattering losses have been determined from these two fluoride glasses which indicate that much smaller losses occur in a fluorozirconate glass ZBL AN than in a thoriated fluoride glass BZL. The scattering losses in ZBL AN at  $\lambda=5145\text{\AA}$  is 20.7 db/km compatible with that in fused quartz (9.94 db/km). These scattering losses are proportional to  $\lambda^{-4}$  and the minimal optical losses are at 2.0-4.0 $\mu$  in fluoride glasses<sup>[42]</sup> and at 1.55 $\mu$  in fused quartz<sup>[9]</sup>. Therefore it can be seen that some fluoride glasses like ZBL AN are extremely promising for

infrared fiber-optical waveguides. Further evidence of more flexible lattices is given by the small values of the  $P_{44}$  photoelastic coefficients. The  $P_{44}$  values of both fluoride samples obtained by us are about 1/6 of the  $P_{44}$  of fused quartz. These small values have not been seen in publications up to now.

Lithium niobate is a very significant material for optical applications. It is a ferroelectric crystal that exhibits large birefringent, pyroelectric, piezoelectric, electro-optic, elastic, photoelastic, and bulk photovoltaic effects. We find that the values of elastic constants  $C_{11}^E$  and  $C_{12}^E$  from a 0.2% Fe doped sample are similar to that from a pure sample. However the Brillouin intensities from 0.2% Fe doped sample are significantly smaller than that from pure sample. This is mainly caused by the much stronger absorption at  $\lambda=5145\text{\AA}$  in the Fe doped sample which has been attributed to intervalence transfer from the  $\text{Fe}^{2+}$  ions to next-nearest-neighbour  $\text{Nb}^{5+}$  ions<sup>[44]</sup>. Further work can be done by using a laser source with a longer wavelength ( $\lambda>6700\text{\AA}$ ) to avoid this absorption band. This will allow a better comparison of the Brillouin intensities between an Fe-doped sample and a pure sample. We obtained the values of acousto-optic figures of merit in a  $35^\circ$  Y-cut pure lithium niobate plate based on the measured photoelastic constants  $P_{31}^E$  and  $P_{41}^E$ . These values obtained by using Brillouin spectroscopy are in good agreement with



the reported values by using other technique<sup>[5]</sup>. We obtained  $M_2 = 7.08 \times 10^{-15} \text{s}^3 \text{kg}^{-1}$  and the reported value is  $M_2 = 6.99 \times 10^{-15} \text{s}^3 \text{kg}^{-1}$ <sup>[5]</sup>.

The work on the room temperature [110] phonon spectra of RADP focused on the concentration dependence of elastic and photoelastic constants. We found that the effective elastic constant  $C = \frac{1}{2}(C_{11} + C_{12}) + C_{66}$  showed a linear increase with increasing ammonium concentration  $x$  while the elastic constant  $C_{44}$  has a nonlinear decrease with  $x$ . We also obtained the photoelastic constants  $P_{31}$ ,  $P_{66}$  and  $P_{44}$ . The results show that  $P_{31}$  decreases with  $\text{NH}_4$  content. The gradually change of its elastic and photoelastic coefficients are expected because RDP and ADP are isomorphic at room temperature having body centered tetragonal unit cells whose volumes are  $v_1 = 424.7 \text{ \AA}$  and  $v_2 = 422.3 \text{ \AA}$ , respectively. These materials form excellent solid solutions at room temperature. As predicted by Nelson and Lax<sup>[33]</sup>, the displacement gradient includes an infinitesimal rigid-body rotation term which will affect the effective photoelastic coefficients  $P_{44}$  and  $P_{55}$  in a birefringent material. We calculated these antisymmetric components of  $P_{44}$  in RADP. Significant corrections are obtained which indicate that the photoelastic coefficient  $P_{44}$  must be expressed as two separate coefficients:  $P_{4,23}$  and  $P_{4,32}$  in RADP.

## REFERENCES

1. Brillouin, L., Ann.de Phys. 17, 88 (1922).
2. Gross, E., Nature 126, 201, 400, 603 (1930).
3. Benedek, G. B., et al., Journ. Opt. Soc. Am. 54, 1284 (1964).
4. Chiao, R. Y. and Stoicheff, B. P., Journ. Opt. Soc. Am. 54, 1286 (1964).
5. Dixon, R.W., J. Appl. Phys., 38, 5145 (1967)
6. Rayleigh, Lord (J.W.Strutt), Proc. Roy. Soc. (London) A95, 476 (1919).
7. Schroeder, J., Light Scattering of Glass, In: Treatise on Materials Science and Technology, Vol. 12 (Academic Press, New York, 1977)
8. Schroeder, J., Fox-Bilmont, M., Pazol, B.G., Tsoukala, V., Drexhage, M.G., El-Bayoumi, O.H., Opt.Eng. 24, 697 (1985)
9. Grishin, I.A., Devyatykh, G.G., Dianov, E.M., Kiselev, N.I., Plotnichenko, V.G., Ritus, A.I., and Churbanov, M.F., Sov. J.Quantum Electron. 17(2), 229 (1987)
10. Matthias, B.T., Remeika, J.P., Phys. Rev. 76, 1886 (1949)

11. Nassau, K., Levinstein, H.J., Loiacono, G.M., J. Chem. Phys. Solids 27, 983 (1966)
12. Nassau, K., Levinstein, H.J., Loiacono, G.M., J. Chem. Phys. Solids 27, 989 (1966)
13. Abrahams, S.C., Reddy, J.M., Bernstein, J.L., J. Chem. Phys. Solids 27, 997 (1966)
14. Abrahams, S.C., Hamilton, W.C., Reddy, J.M., J. Chem. Phys. Solids 27, 1013 (1966)
15. Abrahams, S.C., Hamilton, W.C., Reddy, J.M., J. Chem. Phys. Solids 27, 1019 (1966)
16. O'Brien, R.J., Rosasco, G.J., and Weber, A., In: Light Scattering Spectra of Solids, Edited by Wright, G.B., (Springer-Verlag New York Inc. 1969)
17. Weis, R.S., and Gaylord, T.K., Appl. Phys. A 37, 191 (1985)
18. Courtens, E., J. Phys. (Paris) Lett. 43, L199 (1982)
19. Courtens, E., Vacher, R., and Dagorn, Y., Phys. Rev. B 33, 7625 (1986)
20. Courtens, E., Vacher, R., and Dagorn, Y., Phys. Rev. B 36, 318 (1987)
21. Bouchalkha, A., Master's thesis, Physics, Oklahoma State University, (1989)
22. Kittel, C., Introduction to Solid State Physics, Sixth Edition, (John Wiley & Sons, 1986)
23. Mueller, H., Phys. Rev., 47, 947 (1935)
24. Nye, J.F., Physics Properties of Crystals, (Clarendon, Oxford, 1957)

25. Jackson, J.D., Classical Electrodynamics  
(John Wiley & Sons, 1985)
26. Cummins, H.Z. and Schoen, P.E., in: Laser handbook,  
Vol. 2 edited by Arecchi and Schultz-Dubois,  
pp. 1029-1075. (North-Holland, Amsterdam, 1972)
27. Zallen, R., The Physics of Amorphous Solids,  
(John Wiley & Sons, 1983)
28. Zachariasen, W.H., J. Am. Chem. Soc. 54, 3841 (1932)
29. Elliott, S.R., Physics of Amorphous Materials  
(Longman, London and New York, 1984)
30. Nelson, D.F. and Lax, M., Phys. Rev. B3, 2778 (1971)
31. Chappelle, J. and Taurel, L., Compt. Rend. (Paris) 240,  
743 (1955)
32. Warber, A.W., Onoe, M., and Coquin, G.A., J. Acoust.  
Soc. Am. 42, 1224 (1967)
33. Nelson, D.F., and Lax, M., Phys. Rev. Lett., 24, 379  
(1970)
34. Nelson, D.F., and Lazay, P.D., Phys. Rev., B6, 3109  
(1972)
35. Keyes, R.J., Optical and Infrared Detectors  
(Springer-Verlag, New York, 1980)
36. Kingston, R.H., Detection of Optical and Infrared  
Radiation (Springer-Verlag, New York, 1978)
37. Ota, R. and Soga, N., Non-Cryst. Solids, 56, 105  
(1983)
38. Gangwere, G. H., Ph.D. Thesis, Physics, Oklahoma State  
University, (1989)

39. Mueller, H., Proc. Royal Soc., London, 166A, 425  
(1938)
40. Carleton, H.R., In: Amorphous Materials, Edited by  
Douglas, R.W. and Ellis, B., p.103 (Wiley,  
Interscience, New York, 1972)
41. Schroeder, J., Mohr, R.K., and Macedo, P.B., J. Non-  
Cryst. Solids, 13, 313 (1973-74)
42. Shibata, S., Horiguchi, M., Jinguji, K., Mitachi, S.,  
Kanamori, T., and Manabe, T., Electron. Lett. 17,  
775 (1981)
43. Towner, H. H., Kim, Y. M. and Story, H. S., J. Chem.  
Phys., 56, 3676 (1972)
44. Clark, M. G., Disalvo, F. J., Glass, A. M., and  
Peterson, G. E., J. Chem. Phys. 59, 6209 (1973)
45. Dixon, R.W., and Cohen, M.G., Appl. Phys. Lett., 8,  
205 (1966)
46. Chang, I.C., IEEE Transactions on Sonics and  
Ultrasonics, SU-23, 2-22 (1976)

## APPENDIX A

### THE TRANSMISSION FACTOR ( $f_1$ ) AND THE SOLID ANGLE CORRECTION FACTOR ( $f_2$ )

When the laser light propagates across the surface (1) and the scattered light propagates across surface (2) of the sample (Fig.26), the transmittance  $T$  which is the ratio of transmitted over the incident flux is dependent on the refractive index of the sample. The refractive index is related to the light polarization in the birefringent material.

In our case, the incident light is perpendicular to the sample surface (1) and the scattered light is approximately perpendicular to the surface (2). We ignore the the sample absorption. The transmittance of the incident light at the surface (1) is

$$T_1 = \frac{4 n_1}{(n_1+1)^2} \quad (A-1)$$

where  $n_1$  is the refractive index of sample for the incident light. The transmittance of the scattered light at surface (2) is

$$T_2 = \frac{4 n_s}{(n_s+1)^2} \quad (A-2)$$

where  $n_s$  is the refractive index of sample for the scattered light. Then, the total transmission factor  $f_1$

is

$$f_1 = T_1 \cdot T_2 = \frac{16 n_i n_s}{(n_i + 1)^2 (n_s + 1)^2} \quad (\text{A-3})$$

When the scattered light propagates across the sample surface (2), the direction of the rays are deviated, following Snell's law. This causes a change of the solid angle in which the scattered light was collected. We define the correction factor  $f_2$  as the ratio of collecting solid angle inside the sample over the collecting angle outside the sample. The collecting angle outside the sample is

$$d\Omega_{\text{out}} = 2 \pi \int_0^{\theta_2} \text{SIN } \theta \, d\theta = 2 \pi (1 - \text{COS } \theta_2) \quad (\text{A-4})$$

where  $\theta_2$  is the half angle of the collecting cone outside the sample. For the small angle approximation,

$$1 - \text{COS } \theta_2 = \frac{1}{2} (\theta_2)^2 \quad (\text{A-5})$$

Similar, the solid angle inside the sample is

$$\begin{aligned} d\Omega_{\text{in}} &= 2 \pi \int_0^{\theta_1} \text{SIN } \theta \, d\theta = 2 \pi (1 - \text{COS } \theta_1) \\ &= \pi (\theta_1)^2 \end{aligned} \quad (\text{A-6})$$

where  $\theta_1$  is the half angle of the collecting cone inside the sample. According to Snell's law,

$$n_s \text{ SIN } \theta_1 = n_{\text{air}} \text{ SIN } \theta_2 = \text{SIN } \theta_2 \quad (\text{A-7})$$

For the small angle approximation,

$$n_s \theta_1 = \theta_2 \quad (\text{A-8})$$

Therefore, the solid angle correction factor is

$$f_2 = \frac{d\Omega_{\text{in}}}{d\Omega_{\text{out}}} = \left(\frac{\theta_1}{\theta_2}\right)^2 = \left(\frac{1}{n_s}\right)^2 \quad (\text{A-9})$$

We obtain the total correction factor by multiplying  $f_1$  and  $f_2$ :

$$f = f_1 \cdot f_2 = \frac{16 n_1}{(n_1+1)^2 (n_s+1)^2 n_s} \quad (\text{A-10})$$



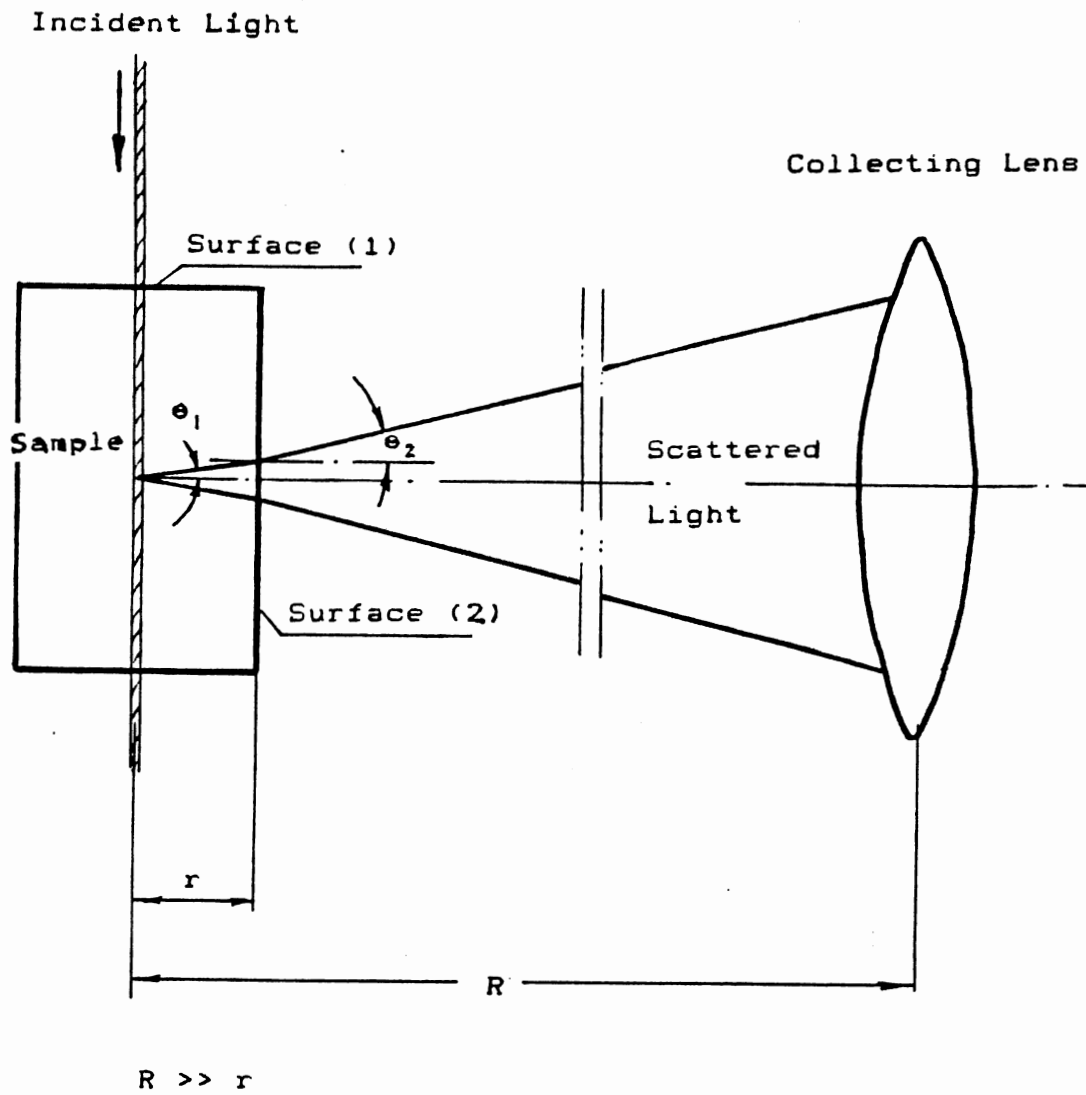


Figure 26. The Transmission and Solid Angle Correction Factors.

## APPENDIX B

### THE FORMULAS FOR DETERMINING THE PHOTOELASTIC CONSTANTS

The photoelastic constants for the samples studied were determined by comparing the measured Brillouin peaks from each of the samples with that of fused quartz. We use fused quartz as a standard sample. The photoelastic constant  $P_{12}$  of fused quartz was given as a reference value in our experiments.

The Brillouin intensity is proportional to the Brillouin scattering cross-section (Rayleigh ratio). It is also proportional to the transmission factor  $f_1$  and the solid angle factor  $f_2$ . Therefore, the ratio of two Brillouin peak intensities will be:

$$\frac{I^i}{I^j} = \frac{R^i f^i}{R^j f^j} \quad (B-1)$$

where  $I$  is the Brillouin peak intensity,  $R$  is the Rayleigh Ratio, and  $f = f_1 \cdot f_2$  is the total correction factor (Appendix A), the superscripts  $i$  and  $j$  specify the special Brillouin peak.

The formulas for determining the photoelastic constants were derived as the follows:

#### 1). Glass

The photoelastic constant  $P_{44}$  of fused quartz was determined by

$$\frac{I_T^0(VH)}{I_L^0(VV)} = \frac{R_T^0(VH)}{R_L^0(VV)} \quad (B-2)$$

using (42) and (43), we obtain

$$P_{44}^0 = \sqrt{2} \left( \frac{I_T^0}{I_L^0} \right)^{1/2} \left( \frac{\Delta\omega_T^0}{\Delta\omega_L^0} \right) P_{12}^0 \quad (B-3)$$

where  $I_T^0$ ,  $I_L^0$  are the Brillouin intensities for the TA and LA peaks.  $\Delta\omega_T^0$ ,  $\Delta\omega_L^0$  are the Brillouin shifts for the TA and LA peaks. The superscript 'o' denotes the measured values from fused quartz.

The photoelastic constant  $P_{12}$  of the fluoride glass was determined by

$$\frac{I_L(VV)}{I_L^0(VV)} = \frac{R_L(VV)}{R_L^0(VV)} \frac{f}{f^0} \quad (B-4)$$

using (10), (42), and (A-10) we obtained

$$P_{12} = \left( \frac{\rho}{\rho^0} \right)^{1/2} \left( \frac{I_L}{I_L^0} \right)^{1/2} \left( \frac{\Delta\omega_L}{\Delta\omega_L^0} \right) \left( \frac{n^0}{n} \right)^5 \frac{(n+1)^2}{(n^0+1)^2} P_{12}^0 \quad (B-5)$$

where  $n^0$  is the index of refraction of fused quartz and  $n$  is the index of refraction of the fluoride glass.

Similarly, the photoelastic constant  $P_{44}$  of the fluoride glass is

$$P_{44} = \left( \frac{\rho}{\rho^0} \right)^{1/2} \left( \frac{I_T(HV)}{I_T^0(HV)} \right)^{1/2} \left( \frac{\Delta\omega_T}{\Delta\omega_T^0} \right) \left( \frac{n^0}{n} \right)^5 \frac{(n+1)^2}{(n^0+1)^2} P_{44}^0 \quad (B-6)$$

## 2). Lithium Niobate

For a birefringent material the refractive indices are different for different polarizations of the light. We modified the form (9) for the case in which the incident light is polarized along the c-axes and the scattered light is polarized perpendicular to c-axes or vice versa. In that case (Fig. 27):

$$|q| = \sqrt{(n_o K_o)^2 + (n_e K_o)^2} = 2 \bar{n} |K_o| \sin\left(\frac{\theta}{2}\right) \quad (\text{B-7})$$

where  $\theta = 90^\circ$  and  $\bar{n} = \sqrt{\frac{1}{2}(n_o^2 + n_e^2)}$ , while  $n_o$  and  $n_e$  are the refractive indices for polarizations  $\perp$  and  $\parallel$  to the c-axes respectively.

We determine the photoelastic constants  $P_{31}$  and  $P_{41}$  of Lithium Niobate from the [100] phonon scattering. Substituting (10), (42), (65) and (A-10) to (B-1) we obtain

$$P_{31} = \left(\frac{\rho}{\rho^0}\right)^{1/2} \left[ \frac{I_L(VV)}{I_L^0(VV)} \right]^{1/2} \left( \frac{\Delta\omega_L(VV)}{\Delta\omega_L^0(VV)} \right) \left( \frac{n^0}{n_e} \right)^5 \frac{(n_e+1)^2}{(n^0+1)^2} P_{12}^0 \quad (\text{B-8})$$

Substituting (10), (42), (66), and (A-10) to (B-1) we obtain

$$P_{41} = \sqrt{2} \left(\frac{\rho}{\rho^0}\right)^{1/2} \left[ \frac{I_L(VH)}{I_L^0(VV)} \right]^{1/2} \left( \frac{\Delta\omega_L(VH)}{\Delta\omega_L^0(VV)} \right) \frac{(n^0)^5}{n(n_e)^2(n_o)^2} \frac{(n_o+1)(n_e+1)}{(n^0+1)^2} P_{12}^0$$

(B-9)

3). RADP.

We determined the photoelastic constants  $P_{31}$ ,  $P_{44}$ ,  $P_{66}$  of RADP from the [110] phonon scattering. Using (10), (42), (82), (A-10), and solving (B-1) we obtain:

$$P_{31} = \left(\frac{\rho}{\rho^0}\right)^{1/2} \left(\frac{I_L(VV)}{I_L^0(VV)}\right)^{1/2} \left(\frac{\Delta\omega_L(VV)}{\Delta\omega_L^0(VV)}\right) \left(\frac{n^0}{n_e}\right)^5 \frac{(n_e+1)^2}{(n^0+1)^2} P_{12}^0$$

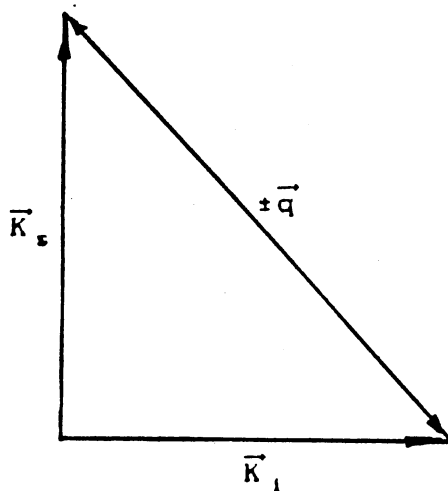
(B-10)

Using (10), (82), (83), (A-10), and solving (B-1) we obtain:

$$P_{44} = \sqrt{2} \left(\frac{I_T(VH)}{I_L(VV)}\right)^{1/2} \left(\frac{\Delta\omega_T(VH)}{\Delta\omega_L(VV)}\right) \frac{(n_e)^3}{n(n_0)^2} \frac{(n_0+1)}{(n_e+1)} P_{31} \quad (B-11)$$

Using (10), (84), (85), (A-10), and solving (B-1) we obtain:

$$P_{66} = \frac{1}{\sqrt{2}} \left(\frac{I_L(HH)}{I_T(HV)}\right)^{1/2} \left(\frac{\Delta\omega_L(HH)}{\Delta\omega_T(HV)}\right) \frac{\bar{n}(n_e)^2}{(n_0)^3} \frac{(n_0+1)}{(n_e+1)} P_{44} \quad (B-12)$$



$$|k_i| = n_e |k_o|$$

$$|k_s| = n_o |k_o|$$

Figure 27. The Relation Among the Wavevectors for the Case in Which the Incident Light is Polarized Along the C-axis While the Scattered Light is Polarized Perpendicular to the C-axis.

$\vec{k}_o$ : the wavevector of light in free space.

VITA

ZHENGDA PAN

Candidate for the Degree of  
Master of Science

**Thesis:** INVESTIGATION OF ELASTIC AND PHOTOELASTIC  
CONSTANTS OF FERROELECTRIC AND GLASS MATERIALS  
USING BRILLOUIN SCATTERING

**Major Field:** Physics

**Biographical:**

**Personal Data:** Born in Shanghai, China, January 26,  
1944, the son of Xinghuang Pan and Xigu Zhu.

**Education:** Graduated from Shanghai School (senior)  
in July, 1962; Received Bachelor of Science  
degree in Engineering Physics from Qinghua  
University, Beijing, China in February, 1968;  
completed the requirements for the Master of  
Science degree at Oklahoma State University in  
December, 1989.

**Professional Experience:** Engineer, Jianshi Chemical  
Fertilizer Plant, Hubei, China, July 1968 to  
December 1977; Instructor, Physics Department,  
Huazhong Institute of Technology, January, 1978  
to March, 1979; Lecturer, Optical Engineering  
Department, Huazhong University of Science and  
Technology, April, 1979 to August, 1986;  
Teaching Assistant, Physics Department, Oklahoma  
State University, August, 1986 to June, 1988;  
Graduate Research Assistant, July, 1988 to  
present. Member of Chinese Institute of  
Electronics (CIE) since 1979. Member of the  
American Physical Society since July, 1989.